1994

Steps Toward Determinaton of the Size and Structure of the Broad-Line Region in Active Galactic Nuclei. V. Variability of the Ultraviolet Continuum and Emission Lines of NGC 3783

G. A. Reichert
NASA Goddard Space Flight Center

P. M. Rodriguez-Pascual
ESA IUE Observatory

D. Alloin
Universite Paris

J. Clavel
Astrophysics Division, ESA

D. Michael Crenshaw
NASA Goddard Space Flight Center

Reichert, G. A.; Rodriguez-Pascual, P. M.; Alloin, D.; Clavel, J.; Crenshaw, D. Michael; Kriss, Gerard A.; Krolik, Julian Henry; Malkan, Matthew A.; Netzer, Hagai; Peterson, Bradley M.; Wamsteker, W.; Altamore, A.; Altieri, B.; Anderson, K. S. J.; Blackwell, J. H. Jr,; Boisson, C.; Brosch, N.; Carone, T. E.; Dietrich, M.; England, M. N.; Evans, I. N.; Filippenko, A. V.; Gaskell, C. Martin; Goad, M.; Gondhalekar., P. M.; Horne, K.; Kazanas, D.; Kol Latschny, W.; Koratkar, A. P.; Koristag, Kirk T.; Macalpine, G. M.; Maoz, D.; Mazeh, T.; Mccollum, B.; Miller, H. Richard; Mendes De Oliveira, C.; O'brien, Paul T.; Pastoriza, M. G.; Pelat, D.; Perez, E.; Perola, G. C.; Pogge, Richard William; Ptak, R. L.; Recondo-Gonzalez, M. C.; Rodriguez-Espinosa, J.; Rosenblatt, E. I.; Sadun, A. C.; Santos-Lleo, M .; Shields, J. C.; Shrader, C. R.; Shull, J. M.; Simkin, S. M.; Sitko, M. L.; Snuders, M. A.J; Sparke, L. S.; Stirpe, G. M.; Stoner, R.; . Storchi-Bergm, T.; Sun, W. H.; Wang, T. F.; Welsh, W. F.; White, R. J.; Winge, C.; and Zhen, W., "Steps Toward Determinaton of the Size and Structure of the Broad-Line Region in Active Galactic Nuclei. V. Variability of the Ultraviolet Continuum and Emission Lines of NGC 3783" (1994). *Faculty Publications, Department of Physics and Astronomy*. 90.
https://digitalcommons.unl.edu/physicsfacpub/90

See next page for additional authors

THE ASTROPHYSICAL JOURNAL, 425:582–608, 1994 April 20

STEPS TOWARD DETERMINATION OF THE SIZE AND STRUCTURE OF THE BROAD-LINE REGION IN ACTIVE GALACTIC NUCLEI. V. VARIABILITY OF THE ULTRAVIOLET CONTINUUM AND EMISSION LINES OF NGC 3783

G. A. REICHERT,[1,2] P. M. RODRÍGUEZ-PASCUAL,[3] D. ALLOIN,[4] J. CLAVEL,[5] D. M. CRENSHAW,[2,6] G. A. KRISS,[2,7] J. H. KROLIK,[7] M. A. MALKAN,[8] H. NETZER,[9] B. M. PETERSON,[10] W. WAMSTEKER,[3] A. ALTAMORE,[11] B. ALTIERI,[5,12] K. S. ANDERSON,[13] J. H. BLACKWELL, JR.,[2,6] C. BOISSON,[4] N. BROSCH,[9] T. E. CARONE,[2,14] M. DIETRICH,[15] M. N. ENGLAND,[2,16] I. N. EVANS,[17] A. V. FILIPPENKO,[2,18] C. M. GASKELL,[19] M. GOAD,[20] P. M. GONDHALEKAR,[21] K. HORNE,[17] D. KAZANAS,[2,22] W. KOLLATSCHNY,[15] A. P. KORATKAR,[2,17] K. T. KORISTA,[17] G. M. MACALPINE,[23] D. MAOZ,[24] T. MAZEH,[9] B. MCCOLLUM,[2,16] H. R. MILLER,[25] C. MENDES DE OLIVEIRA,[26] P. T. O'BRIEN,[20] M. G. PASTORIZA,[27] D. PELAT,[4] E. PÉREZ,[28] G. C. PEROLA,[11] R. W. POGGE,[2,10] R. L. PTAK,[2,29] M. C. RECONDO-GONZÁLEZ,[3] J. RODRÍGUEZ-ESPINOSA,[28] E. I. ROSENBLATT,[30] A. C. SADUN,[2,31] M. SANTOS-LLEÓ,[4] J. C. SHIELDS,[2,10] C. R. SHRADER,[2,32] J. M. SHULL,[33] S. M. SIMKIN,[2,34] M. L. SITKO,[2,35] M. A. J. SNIJDERS,[36] L. S. SPARKE,[37] G. M. STIRPE,[38] R. STONER,[2,29] T. STORCHI-BERGMANN,[27] W.-H. SUN,[39] T. WANG,[40] W. F. WELSH,[2,10,17] R. J. WHITE,[10] C. WINGE,[10,27] AND W. ZHENG[2,7]

Received 1993 June 22; accepted 1993 October 25

ABSTRACT

We report on the results of intensive ultraviolet spectral monitoring of the Seyfert 1 galaxy NGC 3783. The nucleus of NGC 3783 was observed with the *International Ultraviolet Explorer* satellite on a regular basis for a total of 7 months, once every 4 days for the first 172 days and once every other day for the final 50 days. Significant variability was observed in both continuum and emission-line fluxes. The light curves for the continuum fluxes exhibited two well-defined local minima or "dips," the first lasting $\lesssim 20$ days and the second $\lesssim 4$ days, with additional episodes of relatively rapid flickering of approximately the same amplitude. As in the case of NGC 5548 (the only other Seyfert galaxy that has been the subject of such an intensive, sustained monitoring effort), the largest continuum variations were seen at the shortest wavelengths, so that the continuum became "harder" when brighter. The variations in the continuum occurred simultaneously at all wave-

[1] Universities Space Research Association, NASA Goddard Space Flight Center, Code 668, Greenbelt, MD 20771; I: reichert@rosgip.gsfc.nasa.gov.
[2] Guest Observer with the *International Ultraviolet Explorer* satellite.
[3] ESA *IUE* Observatory, P.O. Box 50727, 28080 Madrid, Spain.
[4] Observatoire de Paris, URA173 CNRS, Université Paris 7, 92195 Meudon, France.
[5] ISO Observatory, Astrophysics Division of ESA, ESTEC, Postbus 299, 2200-AG Noordwijk, The Netherlands.
[6] Astronomy Program, Computer Sciences Corporation, NASA Goddard Space Flight Center, Code 681, Greenbelt, MD 20771.
[7] Department of Physics and Astronomy, Johns Hopkins University, Baltimore, MD 21218.
[8] Department of Astronomy, University of California at Los Angeles, Math-Science Building, Los Angeles, CA 90024.
[9] School of Physics and Astronomy and Wise Observatory, Tel-Aviv University, Tel Aviv 69978, Israel.
[10] Department of Astronomy, Ohio State University, 174 West 18th Avenue, Columbus, OH 43210.
[11] Istituto Astronomico dell'Università, Via Lancisi 29, I-00161 Rome, Italy.
[12] European Southern Observatory, La Silla, Casilla 19001, Santiago, Chile.
[13] Department of Astronomy, New Mexico State University, Box 30001, Department 4500, Las Cruces, NM 88003.
[14] Space Sciences Laboratory, University of California at Berkeley, Berkeley, CA 94720.
[15] Universitätssternwarte, Geismarlandstrasse 11, D-3400 Göttingen, Germany.
[16] Computer Sciences Corporation, NASA Goddard Space Flight Center, Code 684.9, Greenbelt, MD 20771.
[17] Space Telescope Science Institute, 3700 San Martin Drive, Baltimore, MD 21218.
[18] Department of Astronomy, University of California at Berkeley, Berkeley, CA 94720.
[19] Department of Physics and Astronomy, University of Nebraska, Lincoln, NE 68588-0111.
[20] Department of Physics and Astronomy, University College London, Gower Street, London WC1E 6BT, UK.
[21] Astrophysics Group, Rutherford Appleton Laboratory, Chilton, Didcot, Oxfordshire OX11 0QX, UK.
[22] Laboratory for High Energy Astrophysics, NASA Goddard Space Flight Center, Code 665, Greenbelt, MD 20771.
[23] Department of Astronomy, University of Michigan, Dennison Building, Ann Arbor, MI 48109-1090.
[24] Institute for Advanced Study, Princeton, NJ 08540.
[25] NASA, Code SZB, Washington, DC 20546, and Department of Physics and Astronomy, Georgia State University, Atlanta, GA 30303.
[26] Department of Astronomy, University of British Columbia, Vancouver, BC, Canada V6T 1W5.
[27] Departamento de Astronomia, Instituto de Física, Universidade Federal do Rio Grande do Sul, Avenido Bento Gonçalves 9500, CP15051, CEP 91500, Porto Alegre, RS, Brazil.
[28] Instituto de Astrofisica de Canarias, E-38200 La Laguna, Tenerife, Spain.
[29] Department of Physics and Astronomy, Bowling Green State University, Bowling Green, OH 43403.
[30] Center for Astrophysics and Space Science, University of California at San Diego, MC C-011, La Jolla, CA 92093.
[31] Department of Physics and Astronomy and Bradley Observatory, Agnes Scott College, Decatur, GA 30030.
[32] Computer Sciences Corporation, NASA Goddard Space Flight Center, Code 668.1, Greenbelt, MD 20771.
[33] Joint Institute for Laboratory Astrophysics and National Institute of Standards and Technology, University of Colorado, Campus Box 440, Boulder, CO 80309.
[34] Department of Physics and Astronomy, Michigan State University, East Lansing, MI 48824.
[35] Department of Physics, M.L. 11, University of Cincinnati, 400 Geology/Physics Building, Cincinnati, OH 45221-0011.
[36] Astronomisches Institut, Universität Tübingen, Waldhauserstrasse 64, D-7400 Tübingen, Germany.
[37] Department of Astronomy, University of Wisconsin, 475 North Charter Street, Madison, WI 53706-1582.
[38] Osservatorio Astronomico di Bologna, Via Zamboni 33, 40126 Bologna, Italy.
[39] Institute of Astronomy, National Central University, Chung-Li, Taiwan 32054, Republic of China.
[40] University of Science and Technology, Hefei, Anhui, People's Republic of China.

lengths ($\Delta t < 2$ days). Generally, the amplitude of variability of the emission lines was lower than (or comparable to) that of the continuum. Apart from Mg II (which varied little) and N V (which is relatively weak and badly blended with Lyα), the light curves of the emission lines are very similar to the continuum light curves, in each case with a small systematic delay or "lag." As for NGC 5548, the highest ionization lines seem to respond with shorter lags than the lower ionization lines. The lags found for NGC 3783 are considerably shorter than those obtained for NGC 5548, with values of (formally) ~ 0 days for He II + O III], and ~ 4 days for Lyα and C IV. The data further suggest lags of ~ 4 days for Si IV + O IV] and 8–30 days for Si III] + C III]. Mg II lagged the 1460 Å continuum by ~ 9 days, although this result depends on the method of measuring the line flux and may in fact be due to variability of the underlying Fe II lines. Correlation analysis further shows that the power density spectrum contains substantial unresolved power over timescales of $\lesssim 2$ days, and that the character of the continuum variability may change with time.

Subject headings: galaxies: active — galaxies: individual (NGC 3783) — galaxies: nuclei — galaxies: Seyfert — ultraviolet: galaxies

1. INTRODUCTION

This contribution is the fifth in a series in which we report on campaigns to explore the central regions of active galactic nuclei (AGNs) through intensive observations of variability in the continuum and emission-line fluxes. It has long been realized that the relationship between line and continuum flux variations can be a powerful tool in unraveling the structure and physical conditions in the broad-line regions (BLRs) in AGNs (e.g., Peterson 1993 and references therein). At any given position in the BLR, the emission-line flux at some time t is a reflection of the continuum at some previous time $t - \tau$, where τ is set by the light-travel time to that position. The emission-line light curve $L(t)$ over the entire BLR is usually assumed to be given by convolution of the continuum light curve $C(t)$ with a transfer function $\Psi(t)$, i.e.,

$$L(t) = \int_{-\infty}^{\infty} \Psi(\tau) C(t - \tau) d\tau \ , \qquad (1)$$

where $\Psi(\tau)$ is determined by the emissivity-weighted geometrical distribution of the line-emitting gas (Blandford & McKee 1982). Given data of high signal-to-noise ratio (S/N), which cover a long enough time interval with sufficiently dense sampling, one can invert the problem and solve for $\Psi(\tau)$ and thus begin to build observationally constrained spatial models of the BLR. Needless to say, obtaining data which fulfill all of these requirements has proved to be an enormously difficult challenge.

One exceptional data set which meets all of these requirements has been obtained for the Seyfert galaxy NGC 5548. This AGN was monitored for 8 months from 1988 December to 1989 August, both in the ultraviolet with the *International Ultraviolet Explorer* (*IUE*) at 4 day intervals (Clavel et al. 1991, hereafter Paper I) and in the optical by a large ground-based consortium on an almost daily basis (Peterson et al. 1991, hereafter Paper II; Dietrich et al. 1993, hereafter Paper IV). Optical observations have continued since the end of the *IUE* monitoring, and the data obtained through 1990 October have been published (Peterson et al. 1992, hereafter Paper III). During the period of intensive *IUE* monitoring, the continuum and line fluxes showed marked variability, which was clearly resolved over the timescale of the observations. The variations in the optical continuum closely tracked those in the ultraviolet, with no measurable time delay ($\Delta t < 2$ days). The largest amplitudes were seen at the shortest wavelengths, so that the continuum became measurably "harder" when brighter. The light curves of the emission lines resembled those of the continuum, after allowances for time delays, or lags, which ranged from essentially zero (N V λ1240, He II λ1640) to longer than 34 days (Mg II λ2798). There was a clear systematic trend in which the highest ionization lines showed both the largest fractional amplitudes of variability and the shortest time lags. There was also some indication that the variations at the highest velocities ($|\Delta v| > 3000$ km s^{-1}) in C IV λ1549 systematically led those in the line "cores" (Clavel 1991). Finally, the time lags derived for separate continuum "events" differed among themselves, and from the time lags derived from the data set as a whole (Netzer & Maoz 1990).

Further discussion and interpretation of these results can be found in a number of subsequent papers (e.g., Crenshaw & Blackwell 1990; Horne, Welsh, & Peterson 1991; Krolik et al. 1991; Collin-Souffrin 1991; Courvoisier & Clavel 1991; Ferland et al. 1992; Pogge & Peterson 1992; Maoz et al. 1993). It is clear that the implications of these data are not yet fully understood. However, it seems fairly safe to conclude that the BLR in NGC 5548 is stratified; that is, the response from the higher ionization lines (e.g., N V, C IV, He II) occurs primarily in regions very close to the continuum source, and the response from the lower ionization lines (e.g., C III] λ1909, Hβ, Mg II, Fe II, the Balmer continuum) is highest in regions farther away from the central source.

A number of other AGNs have also been monitored at optical and UV wavelengths (reviewed by Peterson 1993), but no other source has been the subject of such an intensive, sustained multiwavelength effort. Unfortunately, there is no way of knowing how typical NGC 5548 is of AGNs in general. Most models of the central regions of these sources are not spherically symmetric, and observations of a single source at a single inclination are bound to be incomplete if not misleading.

For these reasons, we have carried out a campaign to monitor intensively a second AGN, the bright, southern Seyfert galaxy NGC 3783. NGC 3783 was chosen because it has a well-documented history of strong UV (Barr, Willis, & Wilson 1983; Chapman, Geller, & Huchra 1985; Marshall, Warwick, & Pounds 1981; Koratkar & Gaskell 1991), optical (Menzies & Feast 1983; de Ruiter & Lub 1986; Stirpe, de Bruyn, & van Groningen 1988; Evans 1989; Winge et al. 1992), infrared (Glass 1992), and X-ray variability (Marshall et al. 1981; McHardy 1988) over timescales as short as 1 week or less. NGC 3783 has prominent broad lines, is bright enough ($m_V \approx 13$ mag) that data of high quality can be obtained in reasonably short integrations, lies far enough above the ecliptic plane that it can be observed continuously with *IUE* for a long period of time, and has a narrow-line region which is not significantly extended (e.g., Winge et al. 1992). The stellar contribution from the host galaxy (a barred spiral; de Vaucouleurs, de Vaucouleurs, & Corwin 1976) to the nuclear optical continuum is also relatively low (e.g., Winge et al. 1992). Finally, the

redshift of NGC 3783 ($z = 0.0097$) is high enough to allow at least a partial separation of the broad Lyα emission from the geocoronal feature in *IUE* spectra.

Other notable properties of NGC 3783 are that its radio emission is unresolved (Unger et al. 1987) and that its X-ray spectrum shows complex and variable absorption at low energies (e.g., Turner et al. 1993). Radio fluxes have been reported by Ulvestad & Wilson (1984) and by Unger et al. (1987).

In this paper, we present results from our *IUE* observations. Further discussion of coordinated observations at other wavelengths will be presented elsewhere (Alloin et al. 1994; Stirpe et al. 1994 hereafter Paper VI), as well as additional analysis and interpretation of these data. Our observations are discussed in § 2. In § 3 we describe the reduction and measurement of the data. Our results are discussed in § 4 and summarized in § 5. Many of the details on the data analysis and measurement are provided in several appendices to this paper; these are intended to supplement the information provided in Paper I and in § 3 of this paper.

2. OBSERVATIONS

2.1. *IUE Observations*

The nucleus of NGC 3783 was observed with *IUE* at a total of 69 separate epochs between 1991 December 21 and 1992 July 29, in the low-dispersion mode (resolution 5–8 Å) and through the large (10″ × 20″) apertures. A total of 118 short-wavelength (SWP, 1150–1980 Å) and 83 long-wavelength (LWP, 1950–330 Å) camera exposures were obtained. (For descriptions of the *IUE* instruments and their performance see Boggess et al. 1978a, b; Faelker, Gordon, & Sandford 1987.) An observing log of the exposures is given in Table 1. Each epoch lasted about 4 hr, except for eight epochs of about 8 hr each. As in the NGC 5548 campaign, the exposure times were chosen to optimize the exposures in the peaks of the strong emission lines. Typically, two SWP exposures and one LWP exposure were obtained during each 4 hr epoch. During the 8 hr epochs we were able to obtain multiple exposures in each camera in order to provide checks on the repeatability and systematic uncertainties of the data.

The observations can be separated into two time intervals of different sampling rate. During the first interval (1991 December 21–1992 June 10), 45 epochs with an average spacing of 4.0 days were obtained. Beginning on 1992 June 10, the observing frequency was doubled, and an additional 24 epochs of average spacing 2.0 days were obtained. Within each interval, the density of epochs was nearly uniform. The spacing of the epochs was decreased in order to allow us to probe the response of the BLR to changes in the continuum over shorter timescales than was possible with NGC 5548.

Care was taken to center the nucleus of NGC 3783 accurately within the aperture, by "locking" the target at the reference point of the Fine Error Sensor (FES) star tracker before moving the target to the aperture. At some epochs, however, this was not possible, due to very high FES background (see below) such that the counts from the target could not be measured. For these epochs, the observations were done as "blind offsets" relative to a nearby bright reference star. The position of the guide star was subsequently used to check the centering of the target. For only two observations was the target not well centered within the aperture: on 1992 January 6 (SWP 43556) and on 1992 January 22 (SWP 43716). Comparison of the flux level of SWP 43556 with that of SWP 43557 (a well-centered image obtained 1 hr later) indicates that ~36.3% of the flux at all wavelengths was lost from SWP 43556. We have therefore not included this spectrum in our analysis. Contour plots of the image from SWP 43726, and the agreement between the resulting wavelength scale and those of other images, indicate that NGC 3783 was still well within the aperture in both the long and the short dimensions, and that virtually no light was lost from this exposure.

The FFS star tracker can also be used to measure broad-band optical fluxes (Holm & Crabb 1979; Barylak, Wasatonic, & Imhoff 1984). Its response curve extends over 4000–7000 Å, with an effective wavelength of ~5000 Å for an AGN-type spectrum. In the "overlap" tracking mode used for our observations, the equivalent aperture of the FES is 12″ × 12″. Hence the underlying stellar population of NGC 3783 contributes significantly to the FES count rates.

Table 1 lists the total (source plus background) and background counts observed by the FES for each observation. Since early 1991, the FES has shown a sharply increased background of scattered light (Teays 1991; Carini 1991), which is strongly dependent on the spacecraft β angle (measured between the target and the antisolar point) and has also varied substantially over both long and short timescales (e.g., Weinstein & Carini 1992b). At some β angles this background can be in excess of 700 counts, far greater than the ~70 counts expected from NGC 3783. Accurate determination of both total and background FES counts was therefore of critical importance.

During these observations, whenever possible we measured the FES counts at the FES reference point, first measuring the total counts with the target at the reference point, and next the background counts after the target had been moved to within the aperture. The counts given represent average readings over typically 300–500 samples. At some epochs, however, it was not possible to obtain a separate background measurement at the reference point. Instead, the FES count rate was monitored as the target was moved, until a drop in count rates was seen as the target entered the aperture. Although this method gives comparable results (Weinstein & Carini 1992a), the counts from the second method were averaged over far fewer samples and hence are less accurate. We have therefore not used these measurements in determining an FES light curve. Finally, for some spacecraft roll angles it was not possible to measure the FES background at all, because of a bright nearby star which was near the reference point when NGC 3783 was within the long-wavelength large aperture.

Table 1 also lists the net FES counts from NGC 3783, after subtraction of the background count rate. Uncertainties were derived according to the procedure discussed in Appendix A, and are the sum in quadrature of the total and background count uncertainties. Net FES counts are given only for the epochs when accurate FES backgrounds could be obtained.

2.2. *HST FOS Observations*

NGC 3783 was observed using the Faint Object Spectrograph (FOS) on the *Hubble* Space Telescope on 1992 July 27, as part of a complementary multiwavelength "World Astronomy Days" program that will be described elsewhere (Alloin et al. 1994). The nucleus of the galaxy was acquired and centered in the 1.″0 aperture on the blue side of the FOS with a binary search. A 2100 s exposure comprised of eight separate readouts was obtained with grating G190H, followed by two 1800 s exposures each comprised of seven separate readouts

TABLE 1

LOG OF *IUE* OBSERVATIONS

IMAGE NUMBER	DATE UT	START TIME (hh:mm:ss)	DURATION (minutes)	JULIAN DATE (2,440,000+)	FES COUNTS			NOTES
					Total	Background	Net	
SWP 43438	1991 Dec 21	10:05:04	80	8611.94796	250	181	69 ± 5.4	
LWP 22043	1991 Dec 21	11:34:54	50	8612.99993	250	175	75 ± 5.4	
SWP 43439	1991 Dec 21	12:30:13	30	8612.03140	...	...	...	
SWP 43472	1991 Dec 25	10:04:36	85	8615.94937	171	97	74 ± 4.8	
LWP 22078	1991 Dec 25	11:36:22	45	8615.99921	...	...	...	
SWP 43473	1991 Dec 25	12:25:56	33	8616.02947	...	...	...	
SWP 43485	1991 Dec 27	14:06:43	85	8618.11751	172	98	74 ± 4.8	
LWP 22101	1991 Dec 27	15:43:35	45	8618.17089	178	111	67 ± 49	
SWP 43539	1992 Jan 2	16:10:35	80	8624.20179	238	...	...	
LWP 22175	1992 Jan 2	17:38:15	40	8624.24878	233	161	72 ± 5.3	
SWP 43540	1992 Jan 2	18:24:05	80	8624.29450	227	...	...	
LWP 22176	1992 Jan 2	19:50:08	40	8624.34037	225	...	...	
SWP 43541	1992 Jan 2	20:35:40	80	8624.38588	216	...	...	
LWP 22177	1992 Jan 2	22:06:04	40	8624.43477	214	148	66 ± 5.2	
SWP 43556	1992 Jan 6	23:32:09	80	8628.50844	220	155	65 ± 5.2	1
LWP 22200	1992 Jan 7	00:59:55	40	8628.55550	214	149	65 ± 5.2	
SWP 43557	1992 Jan 7	01:47:30	60	8628.59549	214	151	63 ± 5.2	
SWP 43587	1992 Jan 10	03:38:56	80	8631.67981	171	105	66 ± 4.8	
LWP 22232	1992 Jan 10	05:10:22	40	8631.72942	173	103	70 ± 4.8	
SWP 43588	1992 Jan 10	05:56:46	50	8631.76512	169	98	71 ± 4.8	
SWP 43636	1992 Jan 14	03:50:01	80	8635.68751	229	164	65 ± 5.3	
LWP 22247	1992 Jan 14	05:21:37	40	8635.73723	230	161	69 ± 5.3	
SWP 43637	1992 Jan 14	06:08:18	40	8635.76965	229	163	66 ± 5.3	
SWP 43676	1992 Jan 18	08:01:22	80	8639.86206	247	180	67 ± 5.4	
LWP 22269	1992 Jan 18	09:28:44	50	8639.91231	...	...	...	2
SWP 43716	1992 Jan 22	10:15:02	60	8643.94794	151	74	77 ± 4.6	3
SWP 43871	1992 Jan 27	20:09:00	80	8649.36736	247	179	68 ± 5.4	
LWP 22289	1992 Jan 27	21:34:10	40	8649.41262	247	185	62 ± 54	
SWP 43872	1992 Jan 27	22:19:57	60	8649.45135	...	...	...	
SWP 43894	1992 Jan 30	05:31:29	80	8651.75797	278	211	67 ± 5.6	
LWP 22304	1992 Jan 30	07:01:40	40	8651.80671	274	206	68 ± 5.6	
SWP 43895	1992 Jan 30	07:51:31	80	8651.85522	277	208	69 ± 5.6	
SWP 43921	1992 Feb 3	14:27:55	80	8656.13050	248	179	69 ± 5.4	4
LWP 22325	1992 Feb 3	16:02:15	40	8656.18212	251	184	67 ± 5.4	
SWP 43922	1992 Feb 3	16:49:33	80	8656.22885	253	181	72 ± 54	
LWP 22326	1992 Feb 3	18:24:57	35	8656.27948	255	181	74 ± 5.4	
SWP 43945	1992 Feb 7	12:19:45	75	8660.03976	207	137	70 ± 5.1	
LWP 22352	1992 Feb 7	13:45:27	35	8660.08538	214	...	...	5
SWP 43946	1992 Feb 7	14:29:58	50	8660.12150	220	152	68 ± 5.2	
SWP 43962	1992 Feb 11	12:31:24	75	8664.04785	213	149	64 ± 5.2	
LWP 22370	1992 Feb 11	13:51:42	35	8664.08972	225	...	...	5
SWP 43963	1992 Feb 11	14:31:52	60	8664.12630	226	158	68 ± 5.3	
SWP 43995	1992 Feb 15	11:54:22	75	8668.02213	200	142	58 ± 5.1	
LWP 22397	1992 Feb 15	13:17:29	40	8668.06770	211	...	...	5
SWP 43996	1992 Feb 15	14:08:26	75	8668.11523	211	150	61 ± 5.2	
SWP 44020	1992 Feb 19	13:55:12	75	8672.10604	195	130	65 ± 5.0	
LWP 22414	1992 Feb 19	15:16:38	40	8672.15044	196	...	...	5
SWP 44021	1992 Feb 19	16:03:37	60	8672.19001	200	136	64 ± 5.1	
SWP 44048	1992 Feb 23	17:54:00	75	8676.27187	177	110	67 ± 4.9	
LWP 22447	1992 Feb 23	19:18:37	40	8676.31848	166	...	...	5
SWP 44049	1992 Feb 23	20:05:37	45	8676.35286	162	95	67 ± 4.7	
SWP 44072	1992 Feb 27	18:49:10	75	8680.31019	140	76	64 ± 4.5	
LWP 22469	1992 Feb 27	20:15:46	40	8680.35817	131	...	...	5
SWP 44099	1992 Mar 2	16:09:32	75	8684.19933	124	58	66 ± 4.3	
LWP 22496	1992 Mar 2	17:35:58	40	8684.24720	133	...	...	5
SWP 44100	1992 Mar 2	18:22:32	27	8684.27502	124	50	70 ± 4.3	
SWP 44126	1992 Mar 6	16:47:53	80	8688.22770	106	44	62 ± 41	
LWP 22523	1992 Mar 6	18:19:04	30	8688.27366	103	44	59 ± 4.1	
SWP 44149	1992 Mar 10	16:21:16	100	8692.21616	89	35	54 ± 3.9	
LWP 22560	1992 Mar 10	18:07:10	40	8692.26887	94	...	...	5
SWP 44176	1992 Mar 14	09:12:24	75	8695.90965	71	16	55 ± 3.5	
LWP 22594	1992 Mar 14	10:32:25	18	8695.94543	73	...	...	
SWP 44189	1992 Mar 18	04:17:17	100	8699.71339	...	...	...	
LWP 22624	1992 Mar 18	06:02:09	45	8699.76712	...	...	...	
SWP 44208	1992 Mar 22	04:30:31	100	8703.72258	64	8	56 ± 3.3	
LWP 22659	1992 Mar 22	06:16:53	45	8703.77735	64	...	...	
SWP 44237	1992 Mar 26	07:59:46	110	8707.87137	66	5	61 ± 3.2	6
LWP 22691	1992 Mar 26	09:56:12	45	8707.92965	...	...	...	6
SWP 44267	1992 Mar 30	04:43:10	100	8711.73137	77	0	77 ± 3.0	
LWP 22713	1992 Mar 30	06:31:45	45	8711.78767	74	...	...	

TABLE 1—*Continued*

Image Number	Date UT	Start Time (hh:mm:ss)	Duration (minutes)	Julian Date (2,440,000+)	FES Counts			Notes
					Total	Background	Net	
SWP 44307	1992 Apr 3	01:50:46	100	8715.61164	75	7	68 ± 3.4	
LWP 22743	1992 Apr 3	03:37:22	45	8715.66657	76	...	...	7
SWP 44308	1992 Apr 3	04:29:45	30	8715.69774	...	...	...	
SWP 44349	1992 Apr 7	09:37:39	90	8719.93240	73	4	69 ± 3.2	
LWP 22760	1992 Apr 7	11:12:51	45	8719.98288	75	5	70 ± 3.3	
SWP 44350	1992 Apr 7	12:05:00	48	8720.02014	74	6	68 ± 3.3	
LWP 22787	1992 Apr 11	10:23:56	45	8723.94891	73	5	68 ± 3.3	
SWP 44381	1992 Apr 11	11:20:17	90	8724.00367	74	5	69 ± 3.3	
SWP 44408	1992 Apr 15	10:28:00	90	8727.96736	73	4	69 ± 3.2	
LWP 22826	1992 Apr 15	12:09:37	40	8728.02057	73	4	69 ± 3.2	
SWP 44409	1992 Apr 15	13:00:29	75	8728.06804	73	6	67 ± 3.3	
LWP 22827	1992 Apr 15	14:26:28	40	8728.11560	74	7	67 ± 3.4	
SWP 44410	1992 Apr 15	15:17:19	90	8728.16828	75	9	66 ± 3.4	
SWP 44434	1992 Apr 19	10:05:11	75	8731.94631	79	6	73 ± 3.4	
LWP 22845	1992 Apr 19	11:30:21	40	8731.99330	77	7	70 ± 3.4	
SWP 44435	1992 Apr 19	12:16:09	40	8732.02510	80	...	...	8
SWP 44461	1992 Apr 23	09:57:12	90	8735.94597	80	9	71 ± 3.5	
LWP 22876	1992 Apr 23	11:35:19	45	8735.99848	82	9	73 ± 3.5	
LWP 22902	1992 Apr 27	10:04:27	45	8739.93538	83	16	67 ± 3.6	
SWP 44486	1992 Apr 27	10:59:56	90	8739.98954	81	16	65 ± 3.6	
SWP 44492	1992 May 1	14:15:23	100	8744.12874	99	28	71 ± 3.9	
LWP 23003	1992 May 1	16:01:47	45	8744.18353	100	32	68 ± 4.0	
SWP 44581	1992 May 5	08:13:32	90	8747.87398	111	40	71 ± 4.1	9
LWP 23035	1992 May 5	10:03:56	45	8747.93502	109	38	71 ± 4.1	
SWP 44627	1992 May 9	07:31:17	90	8751.84464	148	79	69 ± 4.6	
LWP 23073	1992 May 9	09:10:30	45	8751.89792	144	73	71 ± 4.5	
SWP 44628	1992 May 9	10:04:58	85	8751.94963	148	73	75 ± 4.6	
LWP 23074	1992 May 9	11:38:10	45	8752.00046	146	72	74 ± 4.5	
SWP 44629	1992 May 9	12:38:19	85	8752.05612	147	73	74 ± 4.5	
LWP 23075	1992 May 9	14:11:25	40	8752.10515	144	74	70 ± 4.5	
SWP 44659	1992 May 13	08:13:33	85	8755.87226	185	109	76 ± 4.9	
LWP 23094	1992 May 13	09:43:27	40	8755.91906	172	103	69 ± 4.8	10
SWP 44660	1992 May 13	10:31:06	30	8755.94868	182	107	75 ± 4.9	
SWP 44682	1992 May 17	04:08:42	85	8759.70222	223	148	75 ± 5.2	11
LWP 23144	1992 May 20	25:53:11	40	8763.50916	225	156	69 ± 5.2	
SWP 44731	1992 May 21	00:42:20	85	8763.55891	225	165	60 ± 5.3	
LWP 23145	1992 May 21	02:17:49	40	8763.60959	227	163	64 ± 5.3	
SWP 44760	1992 May 25	00:05:47	90	8767.53527	251	182	69 ± 5.4	
LWP 23169	1992 May 25	01:44:42	45	8767.58833	257	186	71 ± 5.4	
SWP 44803	1992 May 29	03:47:09	90	8771.68899	...	...	77	
LWP 23204	1992 May 29	05:24:01	45	8771.74064	...	...	81	
SWP 44804	1992 May 29	06:17:14	30	8771.77238	...	...	75	
SWP 44830	1992 Jun 2	02:25:51	90	8775.63253	286	217	70 ± 5.6	
LWP 23241	1992 Jun 2	04:00:56	45	8775.68294	...	...	...	2
SWP 44873	1992 Jun 6	01:48:49	90	8779.60682	...	...	69	
LWP 23260	1992 Jun 6	03:27:03	45	8779.65941	...	...	71	2
SWP 44874	1992 Jun 6	04:21:03	27	8779.69066	...	...	...	
SWP 44907	1992 Jun 10	10:00:25	90	8783.94821	371	300	71 ± 6.0	
LWP 23280	1992 Jun 10	11:38:41	45	8784.00082	367	294	73 ± 6.0	
SWP 44908	1992 Jun 10	12:23:53	25	8784.02527	...	...	...	
SWP 44918	1992 Jun 12	10:01:25	90	8785.94890	424	352	72 ± 6.3	
LWP 23289	1992 Jun 12	11:48:35	45	8786.00770	...	...	...	
SWP 44921	1992 Jun 14	06:06:44	90	8787.78593	402	325	77 ± 6.2	
LWP 23298	1992 Jun 14	07:41:38	45	8787.83620	398	320	78 ± 6.2	
SWP 44922	1992 Jun 14	08:30:16	29	8787.86442	...	...	...	
SWP 44935	1992 Jun 16	13:58:07	90	8790.11328	383	300	83 ± 6.1	
LWP 23311	1992 Jun 16	15:33:21	45	8790.16378	385	306	79 ± 6.1	
SWP 44936	1992 Jun 16	16:23:41	25	8790.19179	...	...	...	
SWP 44949	1992 Jun 18	05:45:06	85	8791.76917	350	278	72 ± 5.9	
LWP 23318	1992 Jun 18	07:21:09	40	8791.82024	358	288	70 ± 6.0	
SWP 44950	1992 Jun 18	08:15:55	35	8791.85654	357	286	71 ± 6.0	
SWP 44962	1992 Jun 20	05:40:42	85	8793.76611	389	307	82 ± 6.1	
LWP 23329	1992 Jun 20	07:14:39	40	8793.81573	387	312	75 ± 6.1	
SWP 44963	1992 Jun 20	08:03:06	85	8793.86500	383	312	71 ± 6.1	
LWP 23330	1992 Jun 20	09:36:39	40	8793.91434	383	311	72 ± 6.1	
SWP 44964	1992 Jun 20	10:24:13	85	8793.96300	386	313	73 ± 6.1	
LWP 23331	1992 Jun 20	11:57:45	40	8794.01233	379	307	72 ± 6.1	
SWP 44974	1992 Jun 22	05:44:03	85	8795.76844	366	293	73 ± 6.0	
LWP 23352	1992 Jun 22	07:17:24	40	8795.81764	361	287	74 ± 6.0	
SWP 44992	1992 Jun 23	22:03:04	85	8797.44831	349	274	75 ± 5.9	
LWP 23366	1992 Jun 23	23:38:44	40	8797.49912	358	284	74 ± 6.0	

TABLE 1—*Continued*

Image Number	Date UT	Start Time (hh:mm:ss)	Duration (minutes)	Julian Date (2,440,000+)	FES Counts			Notes
					Total	Background	Net	
SWP 44993	1992 Jun 24	00:24:58	60	8797.53817	...	...	...	
SWP 45010	1992 Jun 25	22:17:22	90	8799.45998	344	275	69 ± 5.9	
LWP 23376	1992 Jun 25	23:55:08	45	8799.51225	352	279	73 ± 6.0	12
SWP 45011	1992 Jun 26	00:45:29	30	8799.54200	...	...	...	
SWP 45024	1992 Jun 28	06:05:55	85	8801.78362	502	436	66 ± 6.6	
LWP 23387	1992 Jun 28	07:43:10	40	8801.83553	492	427	65 ± 6.5	
SWP 45025	1992 Jun 28	08:34:40	90	8801.88866	495	421	74 ± 6.5	
LWP 23388	1992 Jun 28	10:15:46	40	8801.94150	399	327	72 ± 6.2	
SWP 45026	1992 Jun 28	11:08:58	90	8801.99581	399	325	74 ± 6.2	
SWP 45038	1992 Jun 29	22:14:31	90	8803.45800	282	...	...	
LWP 23406	1992 Jun 29	23:50:11	45	8803.50881	...	...	...	
SWP 45052	1992 Jul 2	00:16:51	90	8805.54295	249	...	...	
LWP 23416	1992 Jul 2	01:54:27	45	8805.59510	...	...	...	
SWP 45063	1992 Jul 3	23:44:25	90	8807.52043	356	...	...	
LWP 23429	1992 Jul 4	01:21:02	45	8807.57190	...	...	...	
SWP 45064	1992 Jul 4	02:08:25	40	8807.60307	...	...	...	
SWP 45081	1992 Jul 5	23:27:16	90	8809.50852	332	255	77 ± 5.8	
LWP 23449	1992 Jul 6	01:12:01	45	8809.56564	328	255	73 ± 5.8	
SWP 45082	1992 Jul 6	02:04:23	42	8809.60096	334	255	79 ± 5.9	
SWP 45096	1992 Jul 7	23:05:00	90	8811.49306	293	216	77 ± 5.6	
LWP 23466	1992 Jul 8	00:42:00	45	8811.54479	296	217	79 ± 5.7	
SWP 45097	1992 Jul 8	01:46:33	60	8811.59483	295	229	79 ± 5.7	
SWP 45106	1992 Jul 9	20:22:48	100	8813.38389	260	193	67 ± 5.5	
LWP 23475	1992 Jul 9	22:08:56	45	8813.43850	264	193	71 ± 5.5	
SWP 45118	1992 Jul 12	11:57:20	85	8816.02766	264	188	76 ± 5.5	
LWP 23485	1992 Jul 12	13:28:49	40	8816.07557	257	186	71 ± 5.4	
SWP 45119	1992 Jul 12	14:17:25	35	8816.10758	263	184	79 ± 5.5	
SWP 45133	1992 Jul 14	11:52:13	85	8818.02411	263	193	70 ± 5.5	
LWP 23500	1992 Jul 14	13:26:39	45	8818.07580	266	192	74 ± 5.5	13, 14
SWP 45134	1992 Jul 14	14:17:58	30	8818.10623	266	194	72 ± 5.5	
SWP 45150	1992 Jul 16	04:04:49	85	8819.69953	273	196	77 ± 5.5	
LWP 23510	1992 Jul 16	05:36:00	45	8819.74896	267	197	70 ± 5.5	
SWP 45151	1992 Jul 16	06:27:43	90	8819.80050	267	197	70 ± 5.5	
LWP 23511	1992 Jul 16	08:04:48	45	8819.85229	265	196	69 ± 5.5	
SWP 45152	1992 Jul 16	08:56:25	90	8819.90376	267	200	67 ± 5.5	
LWP 23512	1992 Jul 16	10:31:13	20	8819.94529	...	...	...	
SWP 45167	1992 Jul 18	03:50:21	85	8821.68948	276	209	67 ± 5.6	15
LWP 23524	1992 Jul 18	05:23:16	45	8821.74012	277	209	68 ± 5.6	
SWP 45168	1992 Jul 18	06:16:29	85	8821.79096	275	209	66 ± 5.6	
LWP 23525	1992 Jul 18	07:49:32	45	8821.84169	278	204	74 ± 5.6	
SWP 45169	1992 Jul 18	08:42:06	85	8821.89208	278	212	66 ± 5.6	
LWP 23526	1992 Jul 18	10:12:31	35	8821.93751	278	209	69 ± 5.6	
SWP 45194	1992 Jul 20	19:43:42	90	8824.35326	288	...	...	
LWP 23553	1992 Jul 20	21:17:54	45	8824.40306	...	...	...	
SWP 45195	1992 Jul 20	22:06:37	55	8824.44036	...	...	...	
SWP 45206	1992 Jul 22	04:07:09	85	8825.70115	681	609	72 ± 7.1	
LWP 23562	1992 Jul 22	05:39:44	40	8825.74981	674	597	77 ± 7.1	
SWP 45207	1992 Jul 22	06:27:00	85	8825.79826	671	594	77 ± 7.1	
LWP 23563	1992 Jul 22	07:59:51	40	8825.84712	665	591	74 ± 7.1	
SWP 45208	1992 Jul 22	08:48:43	85	8825.89668	675	596	79 ± 7.1	14, 16, 17
LWP 23564	1992 Jul 22	10:20:57	35	8825.94337	676	597	79 ± 7.1	
SWP 45219	1992 Jul 24	08:58:37	85	8827.90355	373	296	77 ± 7.1	
LWP 23573	1992 Jul 24	10:35:28	40	8827.95519	357	286	71 ± 6.0	
SWP 45220	1992 Jul 24	11:27:46	52	8827.99567	359	284	75 ± 6.0	
SWP 45227	1992 Jul 25	18:29:56	90	8829.30204	...	314	...	
LWP 23583	1992 Jul 25	20:11:01	45	8829.35661	...	...	...	
SWP 45237	1992 Jul 27	18:50:48	90	8831.31653	406	...	...	
LWP 23594	1992 Jul 27	20:31:31	45	8831.37084	404	...	...	
SWP 45246	1992 Jul 29	19:04:23	90	8833.32596	438	...	...	
LWP 23601	1992 Jul 29	20:41:58	40	8833.37637	444	...	...	

NOTES.—(1) Target not completely in aperture. (2) Repositioned based on guide star. (3) Target off-center but within aperture. (4) FES counts measured in fast-track/overlap mode. Multiplied by 4.06 to convert equivalents in slow-track/overlap mode. (5) Star too close to reference point to obtain FES background counts. (6) Partial read. (7) New guide star used. (8) Particle hit on spectrum at ~1695 Å. (9) Aperture closed before start of exposure. FES reference point shifted (by less than 1″). (10) Timing problem; no effect on spectrum. (11) Exposed in two segments: 21 minutes 52 s, starting at 04:08:42, plus 63 minutes 8 s, starting at 04:36:58. (12) Extended camera preparation due to overexposure of earlier image. (13) Background high. (14) A few pixels in Mg II λ2798 overexposed. (15) Cosmic-ray "hit" near C IV λ1549. (16) Cosmic-ray "hit" near He II λ1640? (17) One pixel in C IV overexposed.

using grating G130H. The Julian Dates at the beginning of these exposures were 2,448,830.18528, 2,448,830.25119, and 2,448,830.31758, respectively. In order to oversample the response of each diode and to avoid regions with dead diodes, the standard exposure technique of quarter-stepping with an overscan of five diodes was used.

3. DATA REDUCTION AND ANALYSIS

3.1. *Methods of Analysis*

As in the NGC 5548 analysis (Paper I), we have used two independent methods to reduce the ultraviolet spectra and to measure the emission-line and continuum fluxes in order to test the robustness of the measurements and their uncertainties. In the first method, emission-line and continuum fluxes were derived by summing the spectral fluxes from the standard processing over various intervals. The second method used Gaussian extraction and model-fitting techniques similar to those employed in Paper I. For brevity, we shall hereafter use the term SIPS to refer to the first method, and the term GEX to refer to the second.

Both the SIPS and the GEX methods relied on the analysis of the FOS spectrum, the SIPS method for the identification of line-free continuum intervals and the GEX method for definition of the fitted models. The FOS data over the range 1160–2150 Å, shown in Figure 1, were fitted by a model consisting of a power law of the form

$$F_\lambda = F_0\left(\frac{\lambda}{1000}\right)^{-\alpha_\lambda}; \quad (2)$$

extinction using a mean Galactic curve (Seaton 1979); multiple Gaussian components for the emission lines; single Gaussian absorption lines for the known Galactic absorption features; and a damped Lorentzian profile for the strong Galactic Lyα absorption. A more complete description of the analysis is given in Appendix B. Best-fit values for the FOS continuum parameters are summarized in Table 2. The individual fit components are given in Table 3 for the emission lines and in Table 4 for the absorption lines. We emphasize that the model is intended solely as a convenient description of the data, to be used in fitting the *IUE* spectra to determine emission-line and continuum fluxes; we do not necessarily attach physical significance to any of the individual components.

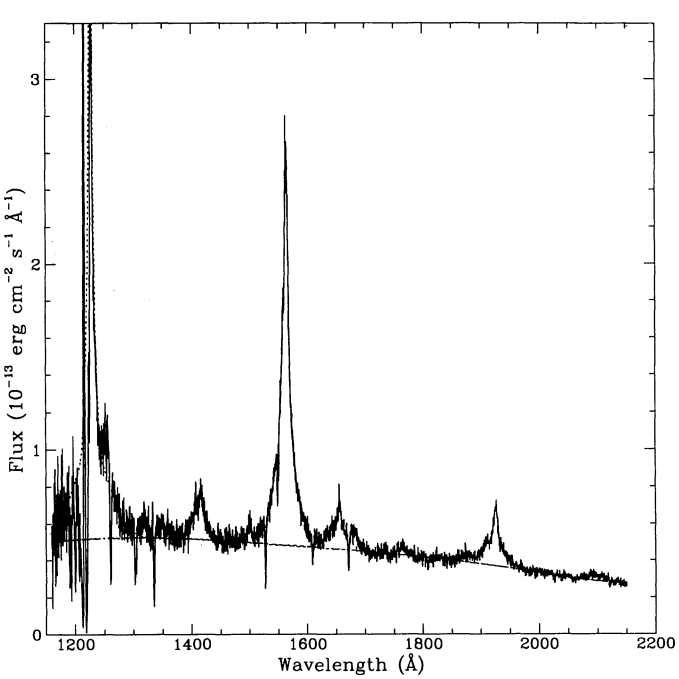

FIG. 1.—Combined FOS spectrum of NGC 3783. The underlying power-law fit to the continuum is shown as the long-dashed line. Also shown (*short-dashed lines*) are the sums of the components for Lyα and He II, to show how these are separated from N V and O III], respectively.

TABLE 2

FOS BEST-FIT CONTINUUM PARAMETERS

Quantity	Value
F_0(1000 Å)[a]	0.622 ± 0.001
Spectral index α_λ	0.694 ± 0.003
E_{B-V}	0.12 ± 0.01
Damped Lyα column	8.39×10^{20} cm^{-2}

[a] Normalizing continuum flux at 1000 Å, in units of 10^{-13} ergs cm^{-2} s^{-1} Å^{-1}.

In the SIPS method, continuum fluxes were measured in three relatively line-free bands, as determined from the FOS spectra. Emission-line fluxes were measured by direct integration above the continuum, which was (except for Si III] + C III]) defined as the straight line passing through two "line-free" bands adjacent to the emission line. Uncertainties for the continuum and emission-line fluxes were derived by computing the standard deviations about the mean fluxes for those epochs with two or more useful exposures. Further details concerning the SIPS method are given in Appendix C.

The second method applied an optimizing extraction method, the modified Gaussian extraction (GEX) technique, to the two-dimensional data, in order to enhance the signal-to-noise ratio and thereby bring out the weaker emission lines. Details of the extraction process are given in Appendix D. Continuum and emission-line fluxes were then derived from multicomponent, least-squares fits to the GEX-extracted spectra. GEX continuum fluxes were measured over the same three bands as for the SIPS fluxes. The template for fitting the SWP spectra was based, with some modification, on the fit obtained for the FOS spectra. In particular, no corrections for reddening were included, as the SWP spectra over the bandpass of the fits (1250–1950 Å) were adequately fitted by a single power law with no extinction correction. The template for fitting the LWP spectra was based on theoretical calculations, and consisted of a power law, plus a synthetic Fe II emission spectrum from Netzer & Wills (1983), plus Gaussian components for the emission and absorption lines. The synthetic Fe II spectrum was convolved with a profile matching the C IV emission line, and additional broad Gaussians were added at 2541, 2815, and 2994 Å to match the data. Further details concerning the spectral fitting of the GEX-extracted spectra are given in Appendix E. Uncertainties in the fitted parameters were derived from the error matrices for each fit (Appendix F).

We note that the GEX power-law fits to the underlying pseudocontinua will still include some contribution from Balmer continuum emission. The difference between the flux in the underlying LWP pseudocontinuum and the integrated flux at 2700 Å suggests that about a third of the integrated flux may be due to Fe II and Balmer continuum, as was found for NGC 5548 (Wamsteker et al. 1990; Maoz et al. 1993). Note also that the GEX fits to the Lyα profiles were determined

TABLE 3

EMISSION LINES IN THE FOS SPECTRUM OF NGC 3783

Feature	λ_{vac} (Å)	Observed Flux (10^{-13} ergs cm^{-2} s^{-1})	Reddening-Corrected Flux (10^{-13} ergs cm^{-2} s^{-1})	cz (km s^{-1})	FWHM (km s^{-1})
Lyα	1215.67	12.00 ± 0.27	35.30 ± 0.79	2893 ± 17	1294 ± 31
Lyα	1215.67	22.20 ± 0.39	65.40 ± 1.15	2917 ± 35	3818 ± 72
Lyα	1215.67	37.00 ± 0.55	109.00 ± 1.62	2745 ± 120	17583 ± 273
Lyα total	...	71.20 ± 0.73	209.70 ± 2.14	...	...
N V	1240.15	4.17 ± 0.17	11.90 ± 0.49	3493 ± 79	3172 ± 149
O I	1302.17	1.19 ± 0.11	3.20 ± 0.31	3253 ± 157	2897 ± 325
C II	1334.53	1.64 ± 0.13	4.30 ± 0.34	2981 ± 260	5333 ± 461
Si IV	1393.76	2.00 ± 0.13	5.07 ± 0.33	2611 ± 94	6102 ± 196
Si IV	1393.76	0.35 ± 0.06	0.88 ± 0.15	2826 ± 59	1192 ± 101
Si IV	1402.77	3.32 ± 0.13	8.40 ± 0.33	2611 ± 0	6102 ± 0
Si IV	1402.77	0.69 ± 0.06	1.75 ± 0.15	2826 ± 0	1192 ± 0
Si IV total	...	6.36 ± 0.20	16.10 ± 0.51	...	...
N IV]	1486.50	0.63 ± 0.06	1.55 ± 0.15	2501 ± 81	1448 ± 147
C IV	1549.05	14.10 ± 0.14	34.00 ± 0.33	2758 ± 8	1714 ± 18
C IV	1549.05	18.00 ± 0.17	43.40 ± 0.42	2468 ± 27	5730 ± 62
C IV	1549.05	16.40 ± 0.21	39.50 ± 0.51	2216 ± 80	12286 ± 187
C IV total	...	48.50 ± 0.30	116.90 ± 0.74	...	...
He II	1640.50	5.34 ± 0.14	12.60 ± 0.33	2211 ± 96	6507 ± 203
He II	1640.50	0.65 ± 0.05	1.54 ± 0.13	2723 ± 40	822 ± 96
He II total	...	5.69 ± 0.15	14.14 ± 0.35	...	...
O III]	1663.00	1.15 ± 0.08	2.71 ± 0.18	3371 ± 85	2247 ± 178
N III]	1750.00	0.72 ± 0.07	1.69 ± 0.16	2450 ± 150	2696 ± 299
Al II	1857.40	1.21 ± 0.08	2.92 ± 0.19	3228 ± 185	4804 ± 354
Si III]	1892.03	2.20 ± 0.07	5.42 ± 0.18	2927 ± 66	3342 ± 129
C III]	1908.73	1.96 ± 0.05	4.88 ± 0.13	2618 ± 20	1352 ± 41
C III]	1908.73	3.20 ± 0.08	8.00 ± 0.21	3828 ± 79	5231 ± 163
C III] total	...	5.16 ± 0.09	12.88 ± 0.25	...	...

almost entirely by the peak and the red wing of the line. The fitting procedure makes a partial, but not complete, correction for the flux lost due to neutral hydrogen absorption in our own Galaxy. We estimate that full correction for this absorption would require an increase of 20%–30% in the fitted Lyα fluxes.

TABLE 4

ABSORPTION LINES IN THE FOS SPECTRUM OF NGC 3783

Feature	λ_{vac} (Å)	Equivalent Width (Å)	cz (km s^{-1})	FWHM (km s^{-1})
Si III	1190.21	...	...	...
Si II	1190.42	0.97 ± 0.10	45 ± 27	401 ± 45
Si II	1193.29	0.90 ± 0.09	28 ± 24	371 ± 45
N I	1199.90	1.60 ± 0.08	50 ± 20	564 ± 33
Si III	1206.50	0.72 ± 0.07	50 ± 23	344 ± 38
Lyα	1215.67	0.81 ± 0.03	2301 ± 8	347 ± 15
Si II	1253.81	0.36 ± 0.05	−50 ± 31	386 ± 54
S II	1259.52	...	...	...
Si II	1260.42	2.08 ± 0.05	19 ± 11	671 ± 18
O I	1302.17	0.73 ± 0.05	7 ± 14	324 ± 24
Si II	1304.37	0.67 ± 0.06	−62 ± 21	392 ± 37
C II	1335.71	...	...	...
C II*	1334.53	1.51 ± 0.05	83 ± 10	458 ± 17
Si IV	1393.76	0.12 ± 0.03	−34 ± 18	150 ± 122
Si IV	1402.77	0.14 ± 0.01	6 ± 43	208 ± 70
Si II	1526.71	1.07 ± 0.05	57 ± 11	366 ± 19
C IV	1548.20	0.48 ± 0.03	39 ± 13	287 ± 25
C IV	1550.77	0.19 ± 0.03	−14 ± 16	176 ± 35
C IV	1549.05	0.98 ± 0.04	2216 ± 22	766 ± 41
Fe II	1608.45	0.59 ± 0.09	84 ± 45	493 ± 90
Al II	1670.79	0.83 ± 0.06	20 ± 19	391 ± 36
Si II	1808.01	0.40 ± 0.07	−18 ± 41	385 ± 78
Al III	1854.72	0.14 ± 0.05	−84 ± 49	218 ± 83
Zn II	2026.14	...	...	...
Mg I	2026.48	0.18 ± 0.04	−41 ± 28	183 ± 48

The SIPS and GEX continuum fluxes at 1460 and 1835 Å, the SWP frequency spectral index α_ν (where $F_\nu \propto \nu^{-\alpha_\nu}$), and the SIPS and GEX fluxes for the Lyα λ1216 + N V λ1240 blend and the C IV λ1549 emission line are listed in Table 5, together with their estimated uncertainties. Note that no attempt has been made to remove the contribution of the many blended low-contrast Fe II lines and Balmer continuum emission (Wills, Netzer, & Wills 1985), so that the values listed for α_ν somewhat overestimate the true spectral index of the continuum emission. The SIPS and GEX fluxes and uncertainties for the weaker SWP emission lines and blends are listed in Table 6. Table 7 lists the 2700 Å integrated continuum and Mg II λ2798 emission-line SIPS and GEX fluxes and uncertainties, as well as the GEX-derived estimates of the fitted power-law fluxes at 2700 Å ($F_{pl,2700}$) and their uncertainties. For all three tables, fluxes for epochs with two or more adequately exposed spectra (as defined in Appendix C) represent the weighted averages over the exposures. The Julian Dates and times of the midpoints of the corresponding exposures are also given in all three tables. For epochs where fluxes from more than one exposure have been averaged, the values given correspond to the midpoints of the time intervals spanned by the individual exposures.

3.2. *Comparison of Results from the Two Methods*

To compare results of the SIPS and GEX measurement procedures, we have performed linear regression analyses (Press & Teukolsky 1992) between the SIPS and GEX fluxes. These results are summarized in Table 8. For each fit the slope and intercept for the best linear fit are given, as well as the linear correlation coefficient r, the minimum reduced χ^2_ν, and the corresponding probability $P(\chi^2_\nu)$ that a correct model would give a value equal to or larger than the observed χ^2_ν. The correlations

TABLE 5

SWP OBSERVATIONS[a]

JULIAN DATE (2,440,000+)	F_{1460}		F_{1835}		α_v	Lyα λ1216 + N V λ1240		C IV λ1549	
	SIPS	GEX	SIPS	GEX	GEX	SIPS	GEX	SIPS	GEX
8611.948	5.41 ± 0.17	5.56 ± 0.15	4.87 ± 0.22	4.73 ± 0.12	1.29 ± 0.03	382 ± 31	678 ± 32	798 ± 33	773 ± 27
8615.949	4.79 ± 0.17	4.94 ± 0.20	4.41 ± 0.22	4.25 ± 0.11	1.34 ± 0.10	327 ± 31	586 ± 33	735 ± 33	711 ± 32
8618.118	4.35 ± 0.17	4.23 ± 0.12	4.16 ± 0.22	3.94 ± 0.10	1.70 ± 0.03	325 ± 31	614 ± 32	746 ± 33	763 ± 27
8624.294	5.41 ± 0.10	5.36 ± 0.14	4.57 ± 0.14	4.50 ± 0.11	1.21 ± 0.03	360 ± 19	625 ± 19	732 ± 20	713 ± 14
8628.595	4.34 ± 0.17	4.20 ± 0.15	3.03 ± 0.22	3.81 ± 0.11	1.57 ± 0.06	347 ± 31	593 ± 32	662 ± 33	693 ± 34
8631.680	3.85 ± 0.17	3.57 ± 0.11	3.51 ± 0.22	3.47 ± 0.09	1.88 ± 0.04	362 ± 31	572 ± 25	642 ± 33	670 ± 23
8635.688	4.47 ± 0.17	4.20 ± 0.12	3.73 ± 0.22	3.67 ± 0.09	1.42 ± 0.04	321 ± 31	529 ± 67	643 ± 33	653 ± 25
8639.862	4.93 ± 0.17	4.92 ± 0.31	4.24 ± 0.22	4.23 ± 0.31	1.34 ± 0.04	311 ± 31	548 ± 33	724 ± 33	668 ± 27
8643.948	5.35 ± 0.17	4.79 ± 0.25	4.39 ± 0.22	4.40 ± 0.13	1.62 ± 0.16	393 ± 31	687 ± 98	726 ± 33	746 ± 33
8649.367	4.88 ± 0.17	4.97 ± 0.15	4.49 ± 0.22	4.36 ± 0.11	1.42 ± 0.05	393 ± 31	667 ± 88	784 ± 33	792 ± 34
8651.807	4.51 ± 0.13	4.44 ± 0.10	3.99 ± 0.17	3.98 ± 0.07	1.51 ± 0.04	332 ± 23	623 ± 25	715 ± 25	725 ± 20
8656.180	5.73 ± 0.13	5.94 ± 0.13	4.77 ± 0.17	4.65 ± 0.09	1.01 ± 0.01	290 ± 23	570 ± 26	673 ± 25	677 ± 26
8660.040	6.29 ± 0.17	5.65 ± 0.19	4.81 ± 0.22	4.77 ± 0.16	1.26 ± 0.01	402 ± 31	665 ± 60	711 ± 33	740 ± 37
8664.048	3.83 ± 0.17	3.94 ± 0.12	3.58 ± 0.22	3.66 ± 0.10	1.68 ± 0.04	354 ± 31	645 ± 45	780 ± 33	723 ± 25
8668.069	2.85 ± 0.13	3.23 ± 0.08	2.97 ± 0.17	3.19 ± 0.06	1.95 ± 0.04	293 ± 23	588 ± 22	663 ± 25	710 ± 24
8672.106	4.16 ± 0.17	3.86 ± 0.12	3.55 ± 0.22	3.53 ± 0.10	1.60 ± 0.05	337 ± 31	578 ± 42	661 ± 33	686 ± 32
8676.272	4.52 ± 0.17	4.57 ± 0.79	4.06 ± 0.22	4.00 ± 0.84	1.42 ± 0.16	299 ± 31	557 ± 64	657 ± 33	675 ± 22
8680.310	4.55 ± 0.17	4.37 ± 0.12	3.87 ± 0.22	3.93 ± 0.10	1.53 ± 0.04	289 ± 31	576 ± 35	702 ± 33	714 ± 29
8684.199	3.28 ± 0.17	3.42 ± 0.16	3.15 ± 0.22	3.27 ± 0.10	1.80 ± 0.14	314 ± 31	523 ± 50	685 ± 33	698 ± 32
8688.228	2.54 ± 0.17	2.60 ± 0.11	2.85 ± 0.22	2.66 ± 0.08	2.10 ± 0.12	249 ± 31	437 ± 32	612 ± 33	591 ± 24
8692.216	2.76 ± 0.17	2.63 ± 0.10	2.69 ± 0.22	2.71 ± 0.13	2.13 ± 0.04	264 ± 31	459 ± 31	652 ± 33	651 ± 28
8695.910	2.30 ± 0.17	2.62 ± 0.08	2.41 ± 0.22	2.63 ± 0.09	2.03 ± 0.01	219 ± 31	453 ± 40	616 ± 33	618 ± 63
8699.713	2.42 ± 0.17	2.45 ± 0.21	2.71 ± 0.22	2.52 ± 0.26	2.13 ± 0.07	225 ± 31	458 ± 37	621 ± 33	611 ± 26
8703.723	2.05 ± 0.17	2.23 ± 0.13	2.44 ± 0.22	2.34 ± 0.06	2.22 ± 0.17	176 ± 31	396 ± 47	589 ± 33	570 ± 26
8707.871	3.09 ± 0.17	3.03 ± 0.15	2.96 ± 0.22	2.92 ± 0.08	1.84 ± 0.13	265 ± 31	467 ± 41	586 ± 33	614 ± 34
8711.731	4.00 ± 0.17	3.79 ± 0.15	3.63 ± 0.22	3.55 ± 0.09	1.71 ± 0.10	286 ± 31	516 ± 31	630 ± 33	638 ± 30
8715.612	4.43 ± 0.17	4.46 ± 0.30	4.18 ± 0.22	4.13 ± 0.33	1.67 ± 0.05	311 ± 31	556 ± 76	686 ± 33	654 ± 22
8719.932	5.05 ± 0.17	4.98 ± 0.14	4.39 ± 0.22	4.24 ± 0.11	1.31 ± 0.03	307 ± 31	591 ± 45	684 ± 33	693 ± 29
8724.004	4.45 ± 0.17	4.57 ± 0.14	4.02 ± 0.22	3.88 ± 0.11	1.29 ± 0.05	318 ± 31	578 ± 52	679 ± 33	638 ± 27
8728.068	4.07 ± 0.10	3.99 ± 0.09	3.69 ± 0.14	3.75 ± 0.07	1.73 ± 0.03	341 ± 19	637 ± 24	738 ± 20	752 ± 20
8731.946	4.55 ± 0.17	4.54 ± 0.15	4.27 ± 0.22	4.04 ± 0.11	1.49 ± 0.07	332 ± 31	660 ± 52	758 ± 33	742 ± 29
8735.946	3.65 ± 0.17	3.79 ± 0.12	3.60 ± 0.22	3.50 ± 0.09	1.66 ± 0.06	335 ± 31	597 ± 42	743 ± 33	718 ± 30
8739.990	3.32 ± 0.17	3.39 ± 0.14	3.32 ± 0.22	3.16 ± 0.09	1.70 ± 0.11	274 ± 31	493 ± 30	667 ± 33	707 ± 30
8744.129	4.34 ± 0.17	3.94 ± 0.18	3.70 ± 0.22	3.62 ± 0.11	1.63 ± 0.14	322 ± 31	492 ± 58	650 ± 33	706 ± 34
8747.874	4.13 ± 0.17	4.26 ± 0.15	3.84 ± 0.22	3.85 ± 0.10	1.56 ± 0.07	339 ± 31	553 ± 24	742 ± 33	719 ± 30
8751.950	4.94 ± 0.10	4.79 ± 0.07	4.45 ± 0.14	4.25 ± 0.06	1.44 ± 0.01	336 ± 19	614 ± 19	717 ± 20	724 ± 19
8755.872	4.51 ± 0.17	4.46 ± 0.26	4.19 ± 0.22	3.82 ± 0.11	1.32 ± 0.19	311 ± 31	606 ± 59	748 ± 33	749 ± 36
8759.702	4.82 ± 0.17	4.76 ± 0.16	4.39 ± 0.22	4.13 ± 0.11	1.38 ± 0.07	288 ± 31	598 ± 38	717 ± 33	688 ± 24
8763.559	4.13 ± 0.17	4.27 ± 0.21	3.97 ± 0.22	3.95 ± 0.12	1.65 ± 0.17	334 ± 31	575 ± 50	713 ± 33	701 ± 110
8767.535	4.22 ± 0.17	4.06 ± 0.12	3.90 ± 0.22	3.75 ± 0.10	1.66 ± 0.04	274 ± 31	569 ± 32	624 ± 33	696 ± 29
8771.689	4.32 ± 0.17	4.33 ± 0.12	3.81 ± 0.22	3.76 ± 0.10	1.38 ± 0.04	245 ± 31	543 ± 36	638 ± 33	643 ± 24
8775.633	4.07 ± 0.17	4.15 ± 0.38	3.65 ± 0.22	3.69 ± 0.40	1.49 ± 0.08	303 ± 31	548 ± 40	693 ± 33	637 ± 65
8779.607	5.19 ± 0.17	5.13 ± 0.22	4.86 ± 0.22	4.61 ± 0.12	1.53 ± 0.11	292 ± 31	554 ± 35	683 ± 33	668 ± 33
8783.948	5.45 ± 0.17	5.20 ± 0.15	4.56 ± 0.22	4.35 ± 0.15	1.22 ± 0.02	322 ± 31	499 ± 27	690 ± 33	674 ± 71
8785.949	5.14 ± 0.17	5.03 ± 0.15	4.63 ± 0.22	4.42 ± 0.11	1.43 ± 0.04	350 ± 31	622 ± 36	689 ± 33	765 ± 31
8787.786	5.27 ± 0.17	5.36 ± 0.14	4.56 ± 0.22	4.61 ± 0.11	1.34 ± 0.03	318 ± 31	549 ± 29	690 ± 33	694 ± 25
8790.113	5.32 ± 0.17	5.52 ± 0.16	4.63 ± 0.22	4.77 ± 0.12	1.36 ± 0.04	263 ± 31	626 ± 31	750 ± 33	746 ± 35
8791.769	5.18 ± 0.17	5.17 ± 0.14	4.50 ± 0.22	4.56 ± 0.12	1.44 ± 0.03	333 ± 31	612 ± 29	756 ± 33	721 ± 27
8793.865	4.88 ± 0.10	4.95 ± 0.09	4.33 ± 0.14	4.29 ± 0.07	1.41 ± 0.03	321 ± 19	547 ± 17	691 ± 20	695 ± 18
8795.768	4.91 ± 0.17	4.93 ± 0.12	4.39 ± 0.22	4.31 ± 0.11	1.41 ± 0.01	325 ± 31	564 ± 35	722 ± 33	708 ± 32
8787.489	5.10 ± 0.17	5.01 ± 0.14	4.34 ± 0.22	4.41 ± 0.11	1.46 ± 0.03	329 ± 31	602 ± 27	716 ± 33	758 ± 37
8799.460	4.63 ± 0.17	4.80 ± 0.15	4.69 ± 0.22	4.21 ± 0.11	1.42 ± 0.05	336 ± 31	645 ± 55	681 ± 33	712 ± 36
8801.891	4.84 ± 0.10	4.70 ± 0.13	4.22 ± 0.14	4.12 ± 0.10	1.44 ± 0.03	299 ± 19	564 ± 22	698 ± 20	729 ± 16
8803.458	5.29 ± 0.17	4.96 ± 0.13	4.53 ± 0.22	4.35 ± 0.11	1.42 ± 0.03	364 ± 31	557 ± 24	699 ± 33	751 ± 31
8805.543	6.03 ± 0.17	5.55 ± 0.16	4.92 ± 0.22	4.91 ± 0.12	1.47 ± 0.04	361 ± 31	723 ± 43	755 ± 33	836 ± 35
8807.520	5.47 ± 0.17	5.47 ± 0.17	4.73 ± 0.22	4.74 ± 0.12	1.38 ± 0.05	376 ± 31	660 ± 30	788 ± 33	760 ± 35
8809.509	5.47 ± 0.17	5.29 ± 0.59	4.59 ± 0.22	4.59 ± 0.62	1.38 ± 0.10	325 ± 31	598 ± 34	743 ± 33	743 ± 27
8811.493	5.14 ± 0.17	5.27 ± 0.37	4.54 ± 0.22	4.57 ± 0.38	1.37 ± 0.05	292 ± 31	567 ± 33	733 ± 33	736 ± 123
8813.384	5.02 ± 0.17	4.95 ± 0.72	4.38 ± 0.22	4.25 ± 0.75	1.34 ± 0.13	331 ± 31	533 ± 26	699 ± 33	704 ± 25
8816.028	5.05 ± 0.17	5.07 ± 0.14	4.37 ± 0.22	4.41 ± 0.12	1.39 ± 0.01	290 ± 31	501 ± 36	677 ± 33	678 ± 29
8818.024	4.41 ± 0.17	3.87 ± 0.16	3.62 ± 0.22	3.58 ± 0.10	1.65 ± 0.10	279 ± 31	492 ± 54	679 ± 33	705 ± 33
8819.803	3.65 ± 0.10	3.62 ± 0.06	3.72 ± 0.14	3.43 ± 0.06	1.64 ± 0.02	245 ± 19	457 ± 15	580 ± 20	597 ± 17
8821.791	4.44 ± 0.10	4.53 ± 0.09	4.12 ± 0.14	4.04 ± 0.07	1.48 ± 0.03	247 ± 19	481 ± 18	646 ± 20	648 ± 18
8824.353	5.86 ± 0.17	5.52 ± 0.24	4.78 ± 0.22	4.45 ± 0.12	1.06 ± 0.12	300 ± 31	486 ± 53	624 ± 33	633 ± 39
8825.799	6.01 ± 0.10	5.95 ± 0.11	5.84 ± 0.14	4.96 ± 0.07	1.20 ± 0.04	277 ± 19	498 ± 14	723 ± 20	715 ± 17
8827.904	6.24 ± 0.17	6.28 ± 0.19	5.42 ± 0.22	5.26 ± 0.13	1.22 ± 0.05	301 ± 31	537 ± 46	720 ± 33	710 ± 33
8829.302	5.30 ± 0.17	5.47 ± 0.15	5.10 ± 0.22	4.85 ± 0.12	1.47 ± 0.03	302 ± 31	557 ± 35	819 ± 33	758 ± 32
8831.317	6.30 ± 0.17	6.36 ± 0.16	5.32 ± 0.22	5.13 ± 0.14	1.06 ± 0.01	304 ± 31	512 ± 26	720 ± 33	689 ± 51
8833.326	7.10 ± 0.17	6.75 ± 0.75	5.46 ± 0.22	5.49 ± 0.73	1.10 ± 0.09	357 ± 31	618 ± 82	752 ± 33	768 ± 24

[a] Values for continuum fluxes are given in units of 10^{-14} ergs cm^{-2} s^{-1} Å^{-1}; for emission lines, in units of 10^{-14} ergs cm^{-2} s^{-1}.

TABLE 6

WEAK EMISSION LINES[a]

JULIAN DATE (2,440,000+)	Si IV λ1400 + O IV] λ1402		He II λ1640 + O III] λ1663		C III] λ1909 + Si III] λ1892		N V λ1240
	SIPS	GEX	SIPS	GEX	SIPS	GEX	GEX
8611.948	87 ± 9	88 ± 6	143 ± 17	134 ± 9	49 ± 9	63 ± 4	39 ± 4
8615.949	68 ± 9	72 ± 7	122 ± 17	133 ± 11	48 ± 9	55 ± 5	46 ± 12
8618.118	58 ± 9	89 ± 7	107 ± 17	111 ± 8	61 ± 9	59 ± 5	42 ± 7
8624.294	77 ± 6	86 ± 3	123 ± 10	166 ± 6	65 ± 6	62 ± 5	48 ± 4
8628.595	84 ± 9	92 ± 10	113 ± 17	162 ± 13	78 ± 9	78 ± 5	19 ± 5
8631.680	69 ± 9	65 ± 5	73 ± 17	114 ± 8	80 ± 9	79 ± 5	56 ± 10
8635.688	58 ± 9	80 ± 7	85 ± 17	111 ± 9	62 ± 9	54 ± 3	47 ± 4
8639.862	63 ± 9	86 ± 6	119 ± 17	140 ± 10	64 ± 9	72 ± 5	47 ± 9
8643.948	67 ± 9	118 ± 14	115 ± 17	179 ± 14	54 ± 9	53 ± 5	62 ± 18
8649.367	91 ± 9	95 ± 7	90 ± 17	143 ± 13	67 ± 9	65 ± 5	62 ± 10
8651.807	82 ± 7	79 ± 5	95 ± 13	104 ± 6	69 ± 7	68 ± 3	45 ± 3
8656.180	64 ± 7	56 ± 5	90 ± 13	151 ± 9	42 ± 7	60 ± 4	62 ± 4
8660.040	70 ± 9	109 ± 9	110 ± 17	134 ± 8	48 ± 9	63 ± 5	42 ± 10
8664.048	87 ± 9	96 ± 7	102 ± 17	138 ± 9	67 ± 9	69 ± 4	48 ± 12
8668.069	72 ± 7	101 ± 6	72 ± 13	79 ± 6	68 ± 7	80 ± 3	32 ± 3
8672.106	77 ± 9	94 ± 8	89 ± 17	121 ± 10	64 ± 9	74 ± 5	43 ± 4
8676.272	78 ± 9	80 ± 9	109 ± 17	102 ± 7	61 ± 9	58 ± 3	35 ± 6
8680.310	74 ± 9	80 ± 5	85 ± 17	110 ± 9	62 ± 9	67 ± 6	41 ± 9
8684.199	95 ± 9	77 ± 8	113 ± 17	109 ± 11	77 ± 9	72 ± 6	54 ± 4
8688.228	66 ± 9	65 ± 7	53 ± 17	53 ± 6	62 ± 9	59 ± 4	38 ± 9
8692.216	62 ± 9	68 ± 5	68 ± 17	71 ± 7	73 ± 9	63 ± 4	46 ± 5
8695.910	72 ± 9	65 ± 14	51 ± 17	90 ± 10	78 ± 9	60 ± 5	57 ± 4
8699.713	62 ± 9	68 ± 5	83 ± 17	78 ± 8	40 ± 9	51 ± 4	46 ± 9
8703.723	65 ± 9	64 ± 6	73 ± 17	55 ± 5	58 ± 9	61 ± 3	49 ± 4
8707.871	67 ± 9	70 ± 8	80 ± 17	100 ± 10	60 ± 9	53 ± 3	57 ± 10
8711.731	58 ± 9	83 ± 8	110 ± 17	147 ± 10	72 ± 9	46 ± 4	53 ± 4
8715.612	83 ± 9	95 ± 5	114 ± 17	139 ± 8	52 ± 9	50 ± 5	100 ± 13
8719.932	68 ± 9	76 ± 6	103 ± 17	115 ± 7	61 ± 9	52 ± 4	46 ± 12
8724.004	60 ± 9	74 ± 6	97 ± 17	122 ± 9	58 ± 9	69 ± 5	35 ± 3
8728.068	83 ± 6	104 ± 3	131 ± 10	158 ± 6	70 ± 6	63 ± 4	51 ± 6
8731.946	80 ± 9	90 ± 7	131 ± 17	156 ± 11	43 ± 9	64 ± 4	48 ± 5
8735.946	77 ± 9	79 ± 7	112 ± 17	118 ± 9	72 ± 9	78 ± 12	19 ± 3
8739.990	88 ± 9	74 ± 6	89 ± 17	83 ± 8	74 ± 9	75 ± 5	61 ± 5
8744.129	70 ± 9	89 ± 8	89 ± 17	103 ± 10	64 ± 9	67 ± 5	40 ± 3
8747.874	76 ± 9	79 ± 8	120 ± 17	132 ± 10	65 ± 9	72 ± 5	83 ± 10
8751.950	64 ± 6	77 ± 3	120 ± 10	147 ± 8	60 ± 6	60 ± 4	54 ± 4
8755.872	58 ± 9	98 ± 16	128 ± 17	127 ± 15	61 ± 9	59 ± 6	36 ± 5
8759.702	77 ± 9	89 ± 8	110 ± 17	165 ± 10	48 ± 9	63 ± 5	31 ± 5
8763.559	89 ± 9	87 ± 9	125 ± 17	141 ± 59	54 ± 9	62 ± 5	56 ± 6
8767.535	47 ± 9	83 ± 7	69 ± 17	87 ± 7	57 ± 9	64 ± 4	48 ± 4
8771.689	91 ± 9	88 ± 6	97 ± 17	107 ± 8	62 ± 9	69 ± 5	33 ± 4
8775.633	74 ± 9	80 ± 5	104 ± 17	116 ± 10	68 ± 9	72 ± 4	34 ± 8
8779.607	86 ± 9	87 ± 9	97 ± 17	118 ± 8	35 ± 9	51 ± 8	89 ± 5
8783.948	63 ± 9	62 ± 9	132 ± 17	125 ± 9	39 ± 9	66 ± 4	25 ± 3
8785.949	85 ± 9	94 ± 8	93 ± 17	125 ± 9	35 ± 9	72 ± 5	61 ± 5
8787.786	73 ± 9	71 ± 6	86 ± 17	108 ± 8	66 ± 9	76 ± 4	37 ± 5
8790.113	71 ± 9	87 ± 8	109 ± 17	164 ± 11	73 ± 9	49 ± 4	30 ± 4
8791.769	94 ± 9	96 ± 7	137 ± 17	130 ± 11	60 ± 9	57 ± 4	37 ± 5
8793.865	61 ± 6	69 ± 4	106 ± 10	124 ± 5	62 ± 6	70 ± 4	23 ± 3
8795.768	104 ± 9	57 ± 7	101 ± 17	113 ± 9	50 ± 9	46 ± 4	36 ± 4
8797.489	72 ± 9	90 ± 4	102 ± 17	131 ± 13	62 ± 9	53 ± 3	63 ± 4
8799.460	58 ± 9	72 ± 7	89 ± 17	111 ± 12	51 ± 9	52 ± 5	24 ± 8
8801.891	58 ± 6	77 ± 2	103 ± 10	114 ± 5	59 ± 6	64 ± 4	41 ± 2
8803.458	74 ± 9	82 ± 7	87 ± 17	122 ± 8	53 ± 9	72 ± 5	27 ± 5
8805.543	77 ± 9	121 ± 9	120 ± 17	160 ± 10	51 ± 9	52 ± 4	59 ± 10
8807.520	105 ± 9	119 ± 9	122 ± 17	161 ± 12	66 ± 9	73 ± 5	61 ± 11
8809.509	94 ± 9	86 ± 3	114 ± 17	145 ± 14	78 ± 9	77 ± 6	28 ± 7
8811.493	85 ± 9	89 ± 4	106 ± 17	144 ± 10	70 ± 9	77 ± 6	88 ± 12
8813.384	56 ± 9	58 ± 4	121 ± 17	120 ± 7	81 ± 9	89 ± 6	32 ± 4
8816.028	41 ± 9	53 ± 4	113 ± 17	110 ± 10	73 ± 9	82 ± 5	31 ± 8
8818.024	61 ± 9	90 ± 10	89 ± 17	83 ± 9	70 ± 9	77 ± 5	29 ± 5
8819.803	54 ± 6	74 ± 4	51 ± 10	59 ± 4	70 ± 6	63 ± 6	33 ± 2
8821.791	59 ± 6	57 ± 2	89 ± 10	91 ± 3	61 ± 6	50 ± 4	42 ± 6
8824.353	71 ± 9	74 ± 12	125 ± 17	132 ± 9	52 ± 9	54 ± 3	16 ± 4
8825.799	63 ± 6	68 ± 4	124 ± 10	142 ± 6	58 ± 6	52 ± 4	19 ± 2
8827.904	79 ± 9	72 ± 7	134 ± 17	140 ± 12	43 ± 9	56 ± 4	31 ± 4
8829.302	101 ± 9	90 ± 6	165 ± 17	137 ± 9	47 ± 9	63 ± 6	39 ± 4
8831.317	82 ± 9	84 ± 11	115 ± 17	133 ± 9	52 ± 9	55 ± 6	25 ± 5
8833.326	77 ± 9	88 ± 9	150 ± 17	158 ± 12	58 ± 9	53 ± 5	41 ± 9

[a] Fluxes in units of 10^{-14} ergs cm^{-2} s^{-1}.

TABLE 7

LWP OBSERVATIONS

JULIAN DATE (2,440,000+)	F_{2700}		$F_{pl,2700}$	Mg II λ2798	
	SIPS	GEX	GEX	SIPS	GEX
8612.000	3.42 ± 0.07	3.36 ± 0.11	2.31 ± 0.20	158 ± 13	82 ± 5
8615.999	3.24 ± 0.07	3.08 ± 0.11	1.82 ± 0.52	157 ± 13	92 ± 7
8618.171	2.95 ± 0.07	2.79 ± 0.10	1.57 ± 0.27	175 ± 13	84 ± 6
8624.342	3.35 ± 0.02	3.14 ± 0.06	2.10 ± 0.13	148 ± 4	84 ± 3
8628.555	3.02 ± 0.07	2.83 ± 0.10	1.73 ± 0.11	168 ± 13	95 ± 10
8631.729	2.76 ± 0.07	2.63 ± 0.09	1.50 ± 0.24	152 ± 13	80 ± 5
8635.737	2.81 ± 0.07	2.67 ± 0.09	1.35 ± 0.21	152 ± 13	84 ± 6
8639.912	3.03 ± 0.07	2.81 ± 0.10	2.16 ± 0.17	163 ± 13	84 ± 5
8649.413	3.23 ± 0.07	3.00 ± 0.10	1.61 ± 0.26	148 ± 13	74 ± 6
8651.807	2.92 ± 0.07	2.79 ± 0.10	1.41 ± 0.18	178 ± 13	91 ± 6
8656.230	3.39 ± 0.03	3.18 ± 0.08	2.10 ± 0.15	142 ± 20	81 ± 4
8660.085	3.34 ± 0.07	3.13 ± 0.11	1.99 ± 0.34	160 ± 13	75 ± 7
8664.090	2.81 ± 0.07	2.61 ± 0.10	1.05 ± 0.35	199 ± 13	90 ± 12
8668.068	2.53 ± 0.07	2.41 ± 0.09	1.64 ± 0.20	181 ± 13	80 ± 6
8672.150	2.84 ± 0.07	2.66 ± 0.10	1.54 ± 0.13	138 ± 13	75 ± 6
8676.318	2.89 ± 0.07	2.73 ± 0.10	2.05 ± 0.22	138 ± 13	55 ± 5
8680.358	3.00 ± 0.07	2.87 ± 0.10	1.71 ± 0.37	132 ± 13	72 ± 6
8684.247	2.70 ± 0.07	2.64 ± 0.10	1.81 ± 0.33	140 ± 13	75 ± 5
8688.274	2.23 ± 0.07	2.22 ± 0.09	1.20 ± 0.19	121 ± 13	74 ± 6
8692.269	2.21 ± 0.07	2.14 ± 0.08	0.97 ± 0.13	155 ± 13	81 ± 6
8695.945	2.42 ± 0.07	2.32 ± 0.15	2.13 ± 0.50	103 ± 13	80 ± 11
8699.767	2.20 ± 0.07	2.10 ± 0.08	1.00 ± 0.13	140 ± 13	72 ± 5
8703.777	2.15 ± 0.07	2.13 ± 0.08	1.23 ± 0.13	138 ± 13	82 ± 5
8707.930	2.38 ± 0.07	2.29 ± 0.10	1.34 ± 0.18	117 ± 13	84 ± 6
8711.788	2.66 ± 0.07	2.62 ± 0.09	1.52 ± 0.14	152 ± 13	76 ± 5
8715.667	2.85 ± 0.07	2.87 ± 0.10	2.42 ± 0.22	144 ± 13	77 ± 5
8719.983	3.04 ± 0.07	3.01 ± 0.10	2.10 ± 0.21	126 ± 13	81 ± 5
8723.949	3.01 ± 0.07	2.94 ± 0.11	1.85 ± 0.22	149 ± 13	85 ± 6
8728.068	2.87 ± 0.06	2.82 ± 0.07	1.79 ± 0.13	157 ± 9	77 ± 4
8731.993	2.98 ± 0.07	2.93 ± 0.10	1.48 ± 0.22	146 ± 13	85 ± 5
8735.998	2.70 ± 0.07	2.73 ± 0.10	1.71 ± 0.22	160 ± 13	78 ± 6
8739.935	2.56 ± 0.07	2.50 ± 0.09	1.13 ± 0.17	156 ± 13	76 ± 6
8744.184	3.16 ± 0.07	3.04 ± 0.11	2.64 ± 0.26	140 ± 13	90 ± 6
8747.935	2.84 ± 0.07	2.85 ± 0.09	1.81 ± 0.24	150 ± 13	88 ± 7
8752.001	3.17 ± 0.06	3.12 ± 0.06	1.89 ± 0.13	154 ± 6	84 ± 3
8755.919	2.92 ± 0.07	2.98 ± 0.12	1.66 ± 0.26	150 ± 13	89 ± 7
8763.559	2.83 ± 0.04	2.87 ± 0.07	1.49 ± 0.16	148 ± 6	91 ± 5
8767.588	2.94 ± 0.07	3.01 ± 0.10	2.27 ± 0.19	159 ± 13	83 ± 5
8771.741	3.07 ± 0.07	3.04 ± 0.10	2.11 ± 0.23	142 ± 13	83 ± 5
8775.683	2.96 ± 0.07	2.94 ± 0.10	1.69 ± 0.16	136 ± 13	85 ± 5
8779.659	3.25 ± 0.07	3.23 ± 0.11	2.33 ± 0.19	161 ± 13	87 ± 6
8784.001	3.00 ± 0.07	3.22 ± 0.11	2.16 ± 0.21	126 ± 13	85 ± 6
8786.008	3.21 ± 0.07	3.18 ± 0.11	1.82 ± 0.17	146 ± 13	82 ± 6
8787.836	3.31 ± 0.07	3.38 ± 0.12	2.25 ± 0.25	145 ± 13	74 ± 5
8790.164	3.54 ± 0.07	3.46 ± 0.14	2.85 ± 0.25	130 ± 13	89 ± 7
8791.820	3.34 ± 0.07	3.31 ± 0.12	2.30 ± 0.23	153 ± 13	95 ± 7
8793.914	3.31 ± 0.02	3.24 ± 0.07	2.13 ± 0.11	148 ± 15	80 ± 3
8795.818	3.23 ± 0.07	3.13 ± 0.11	1.78 ± 0.75	163 ± 13	83 ± 5
8797.499	3.28 ± 0.07	3.24 ± 0.12	2.05 ± 0.27	133 ± 13	79 ± 6
8799.512	2.88 ± 0.07	2.92 ± 0.12	1.57 ± 0.28	178 ± 13	103 ± 8
8801.889	3.14 ± 0.06	3.08 ± 0.08	2.20 ± 0.15	143 ± 3	79 ± 4
8803.509	3.19 ± 0.07	3.17 ± 0.11	1.99 ± 0.29	129 ± 13	89 ± 5
8805.595	3.51 ± 0.07	3.51 ± 0.12	2.04 ± 0.55	171 ± 13	92 ± 6
8807.572	3.45 ± 0.07	3.34 ± 0.12	1.89 ± 0.26	168 ± 13	89 ± 6
8809.566	3.44 ± 0.07	3.38 ± 0.12	2.24 ± 0.42	143 ± 13	81 ± 7
8811.545	3.51 ± 0.07	3.46 ± 0.12	2.09 ± 0.18	143 ± 13	93 ± 6
8813.438	3.50 ± 0.07	3.44 ± 0.12	2.65 ± 0.36	169 ± 13	82 ± 6
8816.076	3.28 ± 0.07	3.23 ± 0.11	1.36 ± 0.34	142 ± 13	80 ± 4
8818.076	3.09 ± 0.07	3.07 ± 0.14	2.56 ± 0.34	125 ± 13	71 ± 7
8819.801	2.96 ± 0.02	2.87 ± 0.08	1.76 ± 0.20	141 ± 10	76 ± 3
8821.837	3.18 ± 0.06	3.09 ± 0.06	2.20 ± 0.12	147 ± 3	73 ± 3
8824.403	3.54 ± 0.07	3.51 ± 0.12	2.62 ± 0.29	129 ± 13	84 ± 7
8825.846	3.82 ± 0.10	3.68 ± 0.07	2.73 ± 0.18	123 ± 11	81 ± 4
8827.955	3.76 ± 0.07	3.72 ± 0.12	2.92 ± 0.24	155 ± 13	86 ± 17
8829.357	3.82 ± 0.07	3.70 ± 0.12	2.57 ± 0.18	146 ± 13	82 ± 6
8831.371	3.73 ± 0.07	3.66 ± 0.12	2.40 ± 0.23	151 ± 13	69 ± 6
8833.376	3.96 ± 0.07	3.94 ± 0.13	2.64 ± 0.34	154 ± 13	78 ± 6

[a] Values for continuum fluxes are given in units of 10^{-14} ergs cm^{-2} s^{-1} Å^{-1}; for emission lines, in units of 10^{-14} ergs cm^{-2} s^{-1}.

TABLE 8

SIPS VERSUS GEX LINEAR REGRESSION[a]

Feature	Slope	Intercept	r	χ^2_ν	$P(\chi^2_\nu)$
F_{1460}	1.049 ± 0.029	-0.18 ± 0.13	0.980	0.779	0.894
F_{1835}	1.132 ± 0.047	-0.44 ± 0.19	0.965	0.755	0.921
F_{2700}	1.020 ± 0.039	-0.010 ± 0.12	0.979	0.485	1.000
Lyα λ1216 + N v λ1240	0.593 ± 0.069	-24 ± 39	0.796	0.518	1.000
Si IV λ1400 + O IV] λ1402	0.679 ± 0.102	17.2 ± 8.2	0.404	1.567	0.002
C IV λ1549	1.030 ± 0.109	-26 ± 77	0.827	0.462	1.000
He II λ1640 + O III] λ1663	0.660 ± 0.071	23.0 ± 8.8	0.724	0.800	0.865
C III] λ1909 + Si III] λ1892	0.665 ± 0.128	18.7 ± 8.2	0.493	1.047	0.340
Mg II λ2798	1.818 ± 0.418	-0.3 ± 35	0.350	1.055	0.325

[a] Values for continuum fluxes are given in units of 10^{-14} ergs cm^{-2} s^{-1} Å^{-1}; for emission lines, in units of 10^{-14} ergs cm^{-2} s^{-1}.

are highly significant in each case, with the exception of the Si IV + O IV] feature, and the probabilities for the linear fits are all of order 30% or higher. The values of the slopes for C IV and the continuum fluxes are all close to unity, and the intercepts are zero to within the uncertainties. We note the following:

1. The SIPS and GEX continuum fluxes in all three bandpasses and the C IV emission-line fluxes are extremely well correlated, and agree for the most part to within the uncertainties. There is a slight tendency for the SIPS continuum fluxes to be a few percent higher than the GEX fluxes, with the largest overall difference occurring in the 2700 Å continuum band.

2. The SIPS fluxes in the Lyα + N V blend fall substantially below the GEX fluxes. This is easily understood, as the GEX fluxes contain contributions from the blue wing of the line and the SIPS fluxes are not corrected for these.

3. While the C IV line fluxes from the two methods are in good agreement, as expected for such a strong and relatively well-isolated emission-line, the weaker SWP lines are not as well correlated. Nevertheless, the agreement between the two methods is still fairly good. There is a tendency for the SIPS values of the weaker lines to fall systematically below the GEX values for higher line fluxes. It appears that this may be in part due to the slightly higher SIPS continuum fluxes, which will have a correspondingly greater effect on the weaker emission lines. For the He II + O III] feature, the trend may be due in part to blending with the red wing of C IV, which is treated differently by the two methods. For the Si III] + C III] feature, some part of the trend might be caused by the different extrapolations of the underlying continuum, coupled with the observed correlation between spectral slope and brightness (see § 4.1). Finally, inspection of Figures 1 and 10 indicates that the presence of weak O I λ1302 may affect the placement of the continuum for the SIPS measurement of Si IV + O IV].

4. The GEX Mg II fluxes fall well below the values determined by SIPS, owing to the fact that the two methods attribute different amounts of the broad spectral "bump" at ~2800 Å to Mg II. The GEX-derived values include no flux from this bump (the LWP fitting template attributes it almost entirely to Fe II), whereas the SIPS values include essentially all of this flux. We estimate that the flux in the broad bump typically makes up about 30%–50% of the SIPS-derived Mg II fluxes.

4. VARIABILITY ANALYSIS

4.1. *Mean Ultraviolet Spectral Properties and the Pattern of Variability*

Before discussing the spectral variability of NGC 3783, we first summarize the mean ultraviolet spectral properties as determined from this monitoring campaign. The average emission-line and continuum fluxes are given in Table 9. The average frequency spectral index as derived from the SWP model fits is $\langle \alpha_\nu \rangle \approx 1.51$. This value represents an effective spectral index, averaged over the SWP bandpass, for the *reddened* UV spectrum. Correction for the adopted value for the Galactic reddening ($E_{B-V} = 0.12$ mag; see Appendix B)

TABLE 9

VARIABILITY PARAMETERS[a]

	MEAN FLUX		χ^2_ν			R_{max}	
FEATURE	SIPS	GEX	SIPS	GEX	GEX*	SIPS	GEX
F_{1460}	4.63	4.30	40.7	49.9	12.5	3.5 ± 0.3	3.0 ± 0.3
F_{1835}	4.15	3.87	12.5	42.9	10.7	2.4 ± 0.2	2.4 ± 0.2
F_{2700}	3.10	2.95	33.4	16.9	16.9	1.8 ± 0.1	1.9 ± 0.1
Lyα λ1216 + N v λ1240	310	554	2.3	4.2	1.9	2.3 ± 0.4	1.8 ± 0.2
Si IV λ1400 + O IV] λ1402	72.0	78.4	2.4	7.3	1.8	2.6 ± 0.6	2.3 ± 0.3
C IV λ1549	697	697	2.9	3.5	1.6	1.4 ± 0.1	1.5 ± 0.1
He II λ1640 + O III] λ1663	104	112	2.2	15.6	1.7	3.2 ± 1.0	3.4 ± 0.6
Si III] λ1892 + C III] λ1909	60.9	62.2	1.5	4.9	0.3	2.3 ± 0.6	2.0 ± 0.2
Mg II λ2798	148	80.8	1.6	1.7	1.7	1.9 ± 0.2	1.9 ± 0.2
N V λ1240	...	38.6	...	14.6	1.1	...	6.2 ± 2.4
Slope α_ν	...	...	...	...	...	...	2.2 ± 0.2
F_{FES}	0.79		...	...	...	1.5 ± 0.3	

[a] Values for continuum fluxes are given in units of 10^{-14} ergs cm^{-2} s^{-1} Å^{-1}; for emission lines, in units of 10^{-14} ergs cm^{-2} s^{-1}.

would give an unreddened effective slope of ~ 0.86. The *intrinsic* continuum in these ranges is likely to be somewhat flatter, however, especially at the longer wavelengths. For example, removal of the Fe II + Balmer continuum from *IUE* spectra of NGC 5548 changes the average dereddened spectral index from ~ 0.95 (Paper I) to ~ 0.4 (Wamsteker et al. 1990; Peterson 1991; Maoz et al. 1993).

The ultraviolet continuum of NGC 3783 varied significantly in both flux and spectral index during the 7 months of our observing campaign. Figure 2 shows light curves of the continuum fluxes and the relative FES flux, which is defined as

$$F_{\rm FES} = 10^{-0.4(V_{\rm FES}-13.0)} . \quad (3)$$

The light curves of the stronger emission lines are shown in Figure 3, and those of the weaker features are shown in Figure 4, together with the light curve of the frequency spectral index. All of these light curves were generated from the GEX measurements, except for the curve showing the SIPS Mg II fluxes.

Table 9 summarizes the variability characteristics of each of the spectral features measured. For each feature we give the mean value over the 7 months of observations, the ratio of maximum to minimum value $R_{\rm max}$, and the value of reduced χ^2_ν (for testing the hypothesis that the flux did not vary):[41] i.e., larger values of χ^2_ν correspond to more significant variability. All quantities were calculated from both the SIPS and the GEX fluxes, and again the agreement between the two methods is quite good, apart from the differences in mean fluxes noted in § 3.4. In addition, because the GEX uncertainties are themselves uncertain, we have also calculated conservative χ^2_ν values for the GEX fluxes (denoted as GEX* in Table 9), multiplying the estimated flux uncertainties by the ratios $\Delta{\rm Flux}_{ij}/\langle\sigma_{\rm GEX}\rangle$ from Table 12.

It is clear from the values of χ^2_ν that significant variations were observed in all of the continuum fluxes, in the spectral index, and in most (if not all) of the emission-line fluxes. With the possible exceptions of Si III] + C III] and N V, the hypothesis of constant flux can be rejected at greater than the 99.9% confidence level ($\chi^2_\nu > 1.6$ for 68 degrees of freedom) even under the most conservative assumptions. The nominal χ^2_ν values indicate that Si III] + C III] and N V probably varied as well, although these results are not as certain as the others because of the low conservative values. In particular, we regard the result for N V as far from conclusive, since the N V fluxes were measured using only one method, and are in any case more dependent on the details of the model fitting than are the other quantities.

It is also clear from Table 9 that the amplitude of variability in the continuum is a function of wavelength, with $R_{\rm max}$ decreasing monotonically with wavelength, from ~ 3.0 at 1460 Å to ~ 1.5 near 5000 Å (FES). As shown in Figure 4, there is a definite trend for the continuum to "harden" as the flux brightens. The values of α_ν mimic the changes in continuum flux epoch by epoch. Formally, we derive a coefficient $r = -0.920$ for the correlation between α_ν and F_{1460}. This behavior is reminiscent of the continuum variations observed in NGC 5548 (Paper I).

[41] In contrast to Papers I–IV in this series, we do not quote the fractional variations $F_{\rm var}$ (defined as the root mean square of the fractional deviations about the mean), since the light curves show substantial time periods when all of the fluxes remained at more or less their average values. The periods of relatively constant flux tend to reduce greatly the value of $F_{\rm var}$; the amplitude of variability tends to be underrepresented by $F_{\rm var}$ if the variations are episodic in nature.

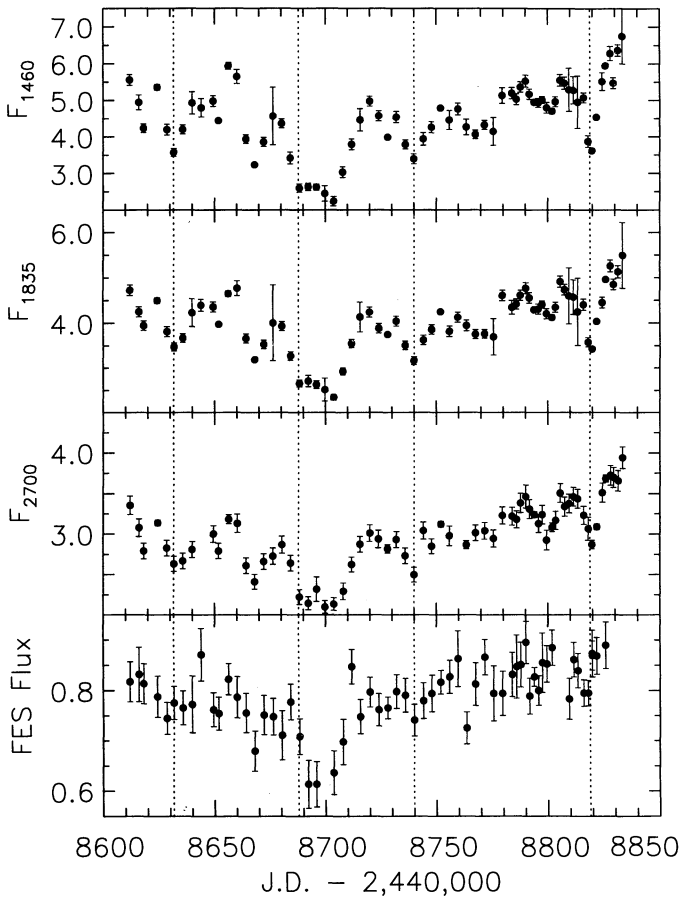

FIG. 2.—Light curves for F_{1460} (*top*), F_{1835} (*upper middle*), integrated F_{2700} (*lower middle*), and relative FES fluxes (*bottom*). All UV fluxes are in units of 10^{14} erg cm^{-2} s^{-1} Å^{-1} and were derived from the GEX plus spectral fitting method. The FES fluxes are as defined in eq. (3). Dashed vertical lines have been drawn to facilitate comparisons with Figs. 3 and 4.

Dilution of the nuclear continuum by stellar emission may account for a substantial fraction of the reduced amplitude of variations in the optical continuum. Dilution by the relatively constant emission from low-constrast Fe II blends and the Balmer continuum can reduce the variability amplitudes at the longer ultraviolet wavelengths, and this dilution must be occurring at some level in NGC 3783. However, the full range in spectral index variations in the SWP range is $\Delta\alpha_\nu \approx 1.1$, with rms fluctuations $\Delta\alpha_\nu \approx 0.16$. If NGC 3783 is similar to NGC 5548 in the properties of the Fe II and Balmer emission, then changes in the Fe II + Balmer pseudocontinuum might cause spectral index changes $\Delta\alpha_\nu \lesssim 0.3$ (Paper I). It seems likely that much of the apparent spectral variability in the ultraviolet continuum is intrinsic. This will be discussed more completely elsewhere (Alloin et al. 1994).

Table 9 also shows that the emission-line fluxes are quite variable as well, with amplitudes which vary from line to line. The largest amplitudes are observed for the lines which are characteristic of highly ionized gases (e.g., $R_{\rm max} \approx 3.4$ for He II). Again, a similar trend was observed for NGC 5548. NGC 3783 is also similar to NGC 5548 in that the variability amplitudes for the emission lines tend to be smaller than those for the continuum fluxes, for all but the highest ionization lines.

The parameter $R_{\rm max}$ is of limited utility, since it contains no temporal information and is subject to large errors. To try to

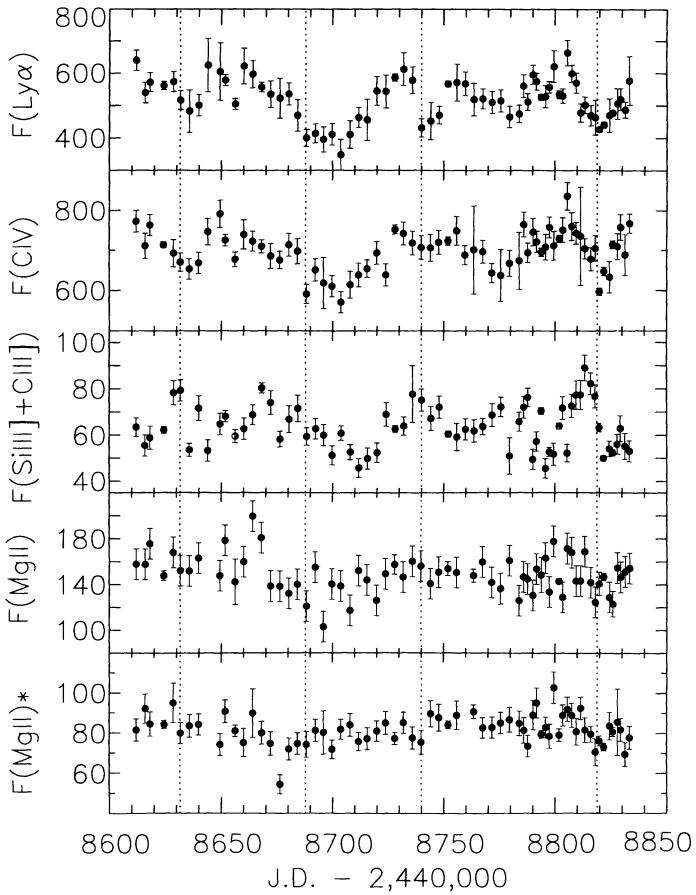

FIG. 3.—Light curves for the GEX-derived Lyα λ1216, C IV λ1549, Si III] λ1892 + C III] λ1909, SIPS-derived Mg II λ2798, and GEX-derived Mg II λ2798 fluxes (*top to bottom*). All fluxes are in units of 10^{-14} ergs cm^{-2} s^{-1}. Dashed vertical lines have been drawn to facilitate comparisons with Figs. 2 and 4.

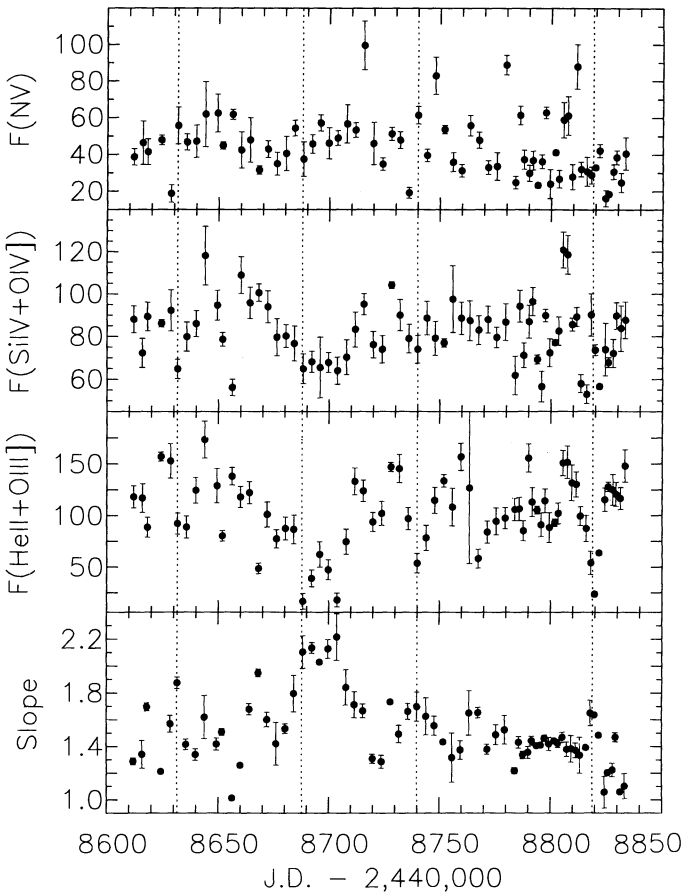

FIG. 4.—Light curves for N V λ1240 (*top*), Si IV + O IV] λ1402 (*upper middle*), and He II λ1640 + O III] λ1663 (*lower middle*) fluxes, and frequency spectral index α_ν (*bottom*). All quantities were derived from the GEX plus spectral fitting method. Fluxes are in units of 10^{-14} ergs cm^{-2} s^{-1}. Dashed vertical lines have been drawn to facilitate comparisons with Figs. 2 and 3.

make a more meaningful comparison of the amplitude of variability for the various features, we have averaged the various light curves over four-epoch bins, using both the SIPS and the GEX fluxes. By averaging over time, we lose information concerning the relatively short-timescale flickering, but gain S/N for studying the longer term variations. Comparisons of various averaged GEX fluxes are illustrated in Figure 5. This figure clearly shows not only that He II + O III] varied by a larger fractional amplitude than did Lyα + N V but also that both features followed the same pattern of variability, with the deviations in He II + O III] consistently of larger amplitude. This is true even when the GEX uncertainties are increased to conservative values using the scaling from Appendix F. Similarly, C IV shows consistently lower amplitude fractional deviations than either He II + O III] or Lyα + N V, while Si IV + O IV] (not shown) is intermediate between He II + O III] and Lyα + N V. Similar conclusions can be drawn from different choices of binning and from comparisons of the averaged SIPS light curves.

The situation for the Si III] + C III] fluxes is not clear as it is for other features. The Si III] + C III] light curve, although noisy if the most conservative error bars are used, shows deviations with the same pattern of variability as seen for F_{1460} and the stronger features, but with amplitude apparently higher than that seen for C IV. In Figure 5, we have anticipated the results of section 4.3 and shifted the Si III] + C III] fluxes to times 12 days earlier (approximately one bin) in order to remove the effects of the emission-line time delay. Even if we do not shift the light curve, it is clear that the Si III] + C III] deviations are not simply *anticorrelated* with the F_{1460} deviations; thus the variations in Si III] + C III] are *not* caused solely by uncertainties in the placement of the underlying continuum. These results indicate that the Si III] + C III] fluxes did show real variability.

The N V fluxes appear to be inconsistent with the pattern of variability set by the other features, even assuming conservative uncertainties. The lack of a cross-check and the sensitivity of the N V fluxes to the details of the modeling renders the N V light curve rather dubious.

4.2. *Detailed Comparison of Emission-Line and Continuum Light Curves*

The continuum light curves obtained for NGC 5548 (Papers I–IV) during the 8 months of *IUE* monitoring showed three large-amplitude "events" (i.e., local maxima in flux preceded and followed by local minima), lasting typically from ~40 to ~100 days, with a few episodes of rapid, small-amplitude variability superposed on the long-term trends. In contrast, the variations observed for NGC 3783 are not so well defined.

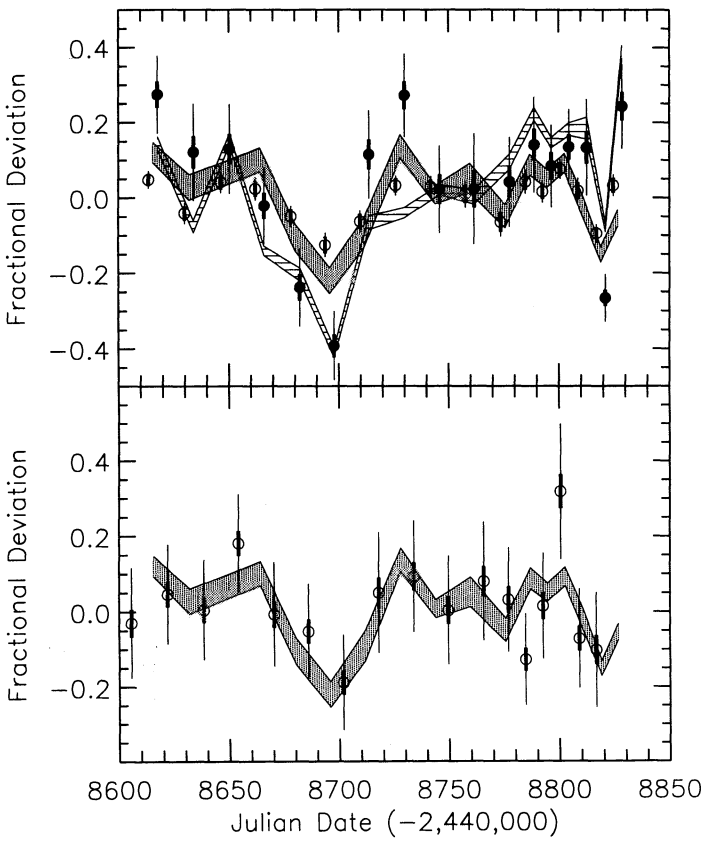

FIG. 5.—Binned light curves for various GEX-derived fluxes. Quantities were averaged every consecutive four measurements. *Top:* Filled and open circles show binned He II + O III] and C IV fluxes, respectively. Thick vertical lines through the circles show the GEX uncertainty estimates, while the longer, thin vertical lines show conservative uncertainties derived by scaling GEX uncertainties by the ratios $\Delta\text{Flux}_{ij}/\langle\sigma_{\text{GEX}}\rangle$ from Table 12. Cross-hatched area shows (GEX) $\pm$ 1 σ limits for binned F_{1460} fluxes; shaded area shows (GEX) $\pm$ 1 σ limits for binned Lyα fluxes. After averaging, the Lyα and C IV light curves were shifted to earlier times by 2 and 4 days, respectively, to account for the effects of the emission-line time delay. *Bottom:* Open circles show binned Si III] + C III] fluxes. Thick and thin vertical lines through the points are as in the top panel. Shaded area shows (GEX) $\pm$ 1 σ limits for binned Lyα fluxes. After averaging, the Si III] + C III] light curve was shifted to times 12 days earlier to remove the emission-line time delay.

From Figure 2, we can separate our 7 months of *IUE* coverage into four distinct time periods, based on the behavior of the continuum fluxes.

1. JD 2,448,612–JD 2,448,680: the continuum fluxes decreased slightly overall, with short ($\sim$8 day) timescale fluctuations about the overall decline.
2. JD 2,448,680–JD 2,448,719: the continuum fluxes decreased rapidly to minimum values, remained low for $\lesssim$20 days, then recovered to approximately the previous levels.
3. JD 2,448,719–JD 2,448,816: the continuum fluxes fluctuated about more or less constant averages, with a sudden increase in average fluxes on about JD 2,448,778 ($\pm$1 day), just before the start of our 2.0 day sampling.
4. JD 2,448,816–JD 2,448,833: the continuum fluxes declined sharply over $\sim$2–4 days to local minima, remained low for $\lesssim$4 days, then increased to maximum values at the end of the monitoring.

The light curves for all of the continuum bandpasses show more or less the same behavior, with differing amplitudes of variability. There are in addition several instances when clearly significant continuum variations (i.e., in excess of the measurement uncertainties) occurred over timescales too short to be resolved, even during the period of 2 day sampling. It is worth noting that, for NGC 3783, the relatively rapid continuum "flickering" (e.g., seen during the first time period) is of approximately the same amplitude as the longer term decrease or "dip" (during the second time period), in contrast to the continuum variability behavior observed with NGC 5548 (Paper I).

As in the case of NGC 5548, the light curves of the strongest emission lines showed marked similarities to the continuum light curves, with some differences. The emission-line light curves all show the initial relatively rapid fluctuations and subsequent broad dip in flux seen in the continuum fluxes. However, the dip in Si III] + C III] appears to be delayed by $\sim$8 days with respect to the other lines, and the dip in He II + O III] appears to show a reversal, in which the flux increases before dipping again. There is also some indication that the fluctuations in Lyα + N V and C IV may have been of lower amplitude than those in the other features, in agreement with the averaged light curves in Figure 5. Most of the emission-line light curves also show dips corresponding to the narrower, secondary continuum dips, although the dips in Lyα + N V and C IV appear to have been largely "washed out." In contrast, the light curves for Mg II and N V do not resemble the continuum light curves. Both the SIPs- and GEX-derived Mg II fluxes were relatively constant over our *IUE* campaign, and, as indicated above, the reliability of the N V measurements is doubtful.

4.3. *Time-Series Analysis*

We expect that the various continuum and emission-line fluxes will be clearly correlated, but with time delays or "lags" attributable to light travel-time effects in the BLR. Such delays can be quantified by performing simple cross-correlation analysis of the light curves. Cross-correlation of time series of astronomical observations is rarely straightforward because the observations are almost never regularly spaced. The data obtained in this project and in our earlier NGC 5548 project (Paper I) are notable exceptions to this generalization. Inspection of Figures 2–4 shows that for NGC 3783 the mean response times of the strong emission lines must be quite short, even relative to our mean sampling intervals. Moreover, due to the change in sampling interval (from 4 days for the first 172 days, to 2 days for the final 50 days), simple cross-correlation analysis requires either that some of the data be excluded (e.g., every other epoch of the final 24) or that the two time intervals be analyzed separately. In this paper we restrict ourselves to relatively simple analyses of the data, based on correlation functions. More detailed interpretation will follow in later work.

We have divided the data into two overlapping subsets: (1) a series of effective 4 day sampling, which covers the entire 7 months of monitoring and excludes every other epoch during the last 2 months, and (2) a series of approximately 2 day sampling which covers only the last 2 months. The two subsets contain 56 and 26 epochs, respectively. The light curves for each of these subsets were analyzed separately. However, although the sampling intervals within each subset were nearly uniform, they were not *precisely* so; slight differences of up to $\sim\frac{2}{3}$ day are sometimes present. Consequently, to compute

correlation functions, we must find some way to make up for this unevenness.

We have employed two different correlation methods in our analysis of each subset. The first is based on the interpolation method proposed by Gaskell & Sparke (1986), while the second is a modification of the discrete correlation method presented by Edelson & Krolik (1988). Each method makes up for the sampling unevenness in a different way. Details of each method are given below, followed by comparison and interpretation of the results.

4.3.1. *Interpolation Method*

Our first method of analysis is based on the interpolation method of Gaskell & Sparke (1986). We have employed the specific implementation described by Gaskell & Peterson (1987) but have not "padded" the light curves beyond their endpoints with any kind of extrapolation. In this method, the regular temporal sampling required for cross-correlation analysis is achieved by interpolating the light curves one at a time between the real observations in a piecewise linear fashion. First, the value of the cross-correlation function (CCF) at any arbitrary lag τ is computed by pairing each of the actual data points in the second light curve at some time t with the interpolated value of the first light curve at time $t - \tau$, for all points for which pairs exist within the real limits of the light curves. The CCF is then computed again, this time by matching the real data points in the first light curve with corresponding interpolated values in the second light curve for time $t + \tau$. The final CCF is then formed by averaging the results of these two computations.

As a check on the interpolation method, we have also computed the sampling window autocorrelation function (ACF) for the SWP data. The sampling window ACF is computed by sampling "white-noise" light curves in the same pattern as the real observations, computing the ACF for these simulated data, and then averaging the ACFs from a large number of such computations. Since the actual data points in these simulations are completely uncorrelated, the width of the peak in the sampling window ACF at small lags shows how much artificial point-to-point correlation is introduced by the interpolation process used. If the sampling window ACF is significantly narrower than the continuum ACF, then this indicates that the dominant variability has been resolved.

4.3.2. *Discrete Method*

Our second method of analysis is based on the discrete correlation method of Edelson & Krolik (1988). This method deals with the problem of uneven sampling by including in the correlation amplitude contributions from only those pairs of fluxes whose time differences are sufficiently close to τ. In essence, this method assumes smoothness in the correlation function over timescales shorter than the sampling interval. We follow a procedure which is very similar to that presented in Edelson & Krolik (1988), but which differs in several technical particulars:

1. We did not weight the data points in their contributions to the correlation functions.

2. Correlation amplitudes were normalized to the total standard deviation and not to the "adjusted" standard deviation (i.e., the quadrature difference between the standard deviation and the rms error). For some fluxes the rms error is a significant fraction of the total standard deviation, and in such cases the normalizations of the correlation functions would be very sensitive to uncertainties in the value of the rms error.

Uncertainties in the correlation amplitudes were derived following the procedure of Edelson & Krolik (1988).

4.3.3. *Comparison and Interpretation of Results*

We first discuss the results obtained with the 4 day data set. In the following, we refer to the results of the interpolation method as cross-correlation functions (hereafter CCFs), and to the results of the discrete method as discrete correlation functions (hereafter DCFs). Also, except where noted, all of the results reported here are based on the GEX values; the results based on the SIPS-extracted data are found to be virtually identical for all of the strong features.

In Figure 6, we show the CCFs and DCFs generated by cross-correlation of the 1460 Å continuum fluxes with the continuum fluxes measured in other bands, and in Figure 7 we show the cross-correlations for the 1460 Å continuum and various of the emission lines. The characteristics of the CCFs are summarized in Table 10; here Δt(peak) refers to the location of the maximum of the cross-correlation function r_{max}.

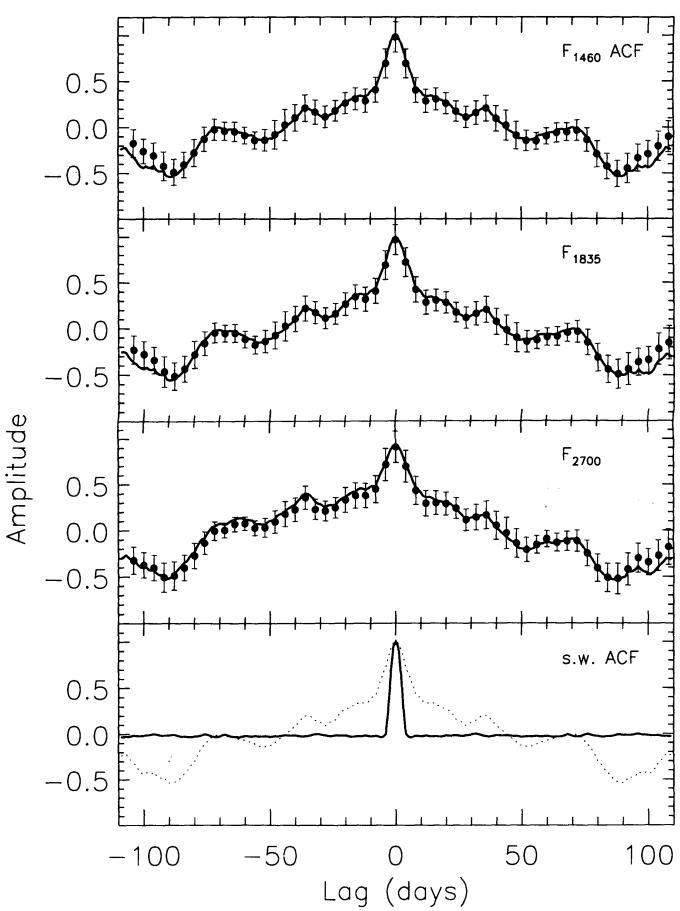

FIG. 6.—Correlations of various continuum fluxes with the continuum flux at 1460 Å, based on the 4 day sampling. All fluxes were derived from the GEX plus spectral fitting method. Solid lines show the correlation amplitudes derived using the interpolation (CCF) method. Solid circles with error bars show the correlation amplitudes and uncertainties derived using the discrete correlation function (DCF) method. *Top to bottom:* autocorrelation function (ACF) for the 1460 Å continuum, and cross-correlations of the continuum fluxes at 1835 and 2700 Å. The bottom panel shows the ACF (*dashed line*) as well as the sampling window ACF for the SWP data (*solid line*), which shows how much artificial point-to-point correlation is introduced by the interpolation process (see text). Note the similarity between the cross-correlation and autocorrelation functions, and the agreement between the CCF and DCF methods.

TABLE 10

CROSS-CORRELATION RESULTS

FEATURE	Δt(peak) (days) SIPS	Δt(peak) (days) GEX	Δt(center) (days) SIPS	Δt(center) (days) GEX	r_{max} SIPS	r_{max} GEX	FWHM (days) SIPS	FWHM (days) GEX	COMMENTS
F_{1460}	0	0	0.0	0.0	1.000	1.000	13.5	14.2	Autocorrelation
F_{1835}	0	0	−0.1	0.1	0.954	0.986	14.7	14.7	
F_{2700}	0	0	0.3	−1.4	0.936	0.932	15.5	18.5	
He II λ1640 + O III] λ1663	1	1	1.1	0.5	0.650	0.669	10.0	11.3	
Si IV λ1400 + O IV] λ1402	3	5	5.3	3.9	0.295	0.297	12.4	13.5	$P \approx 99\%$
Lyα + N V	2	4	4.7	3.8	0.663	0.627	19.1	15.6	
Lyα	...	5	...	4.6	...	0.672	...	16.2	
C IV λ1549	3	5	3.9	5.5	0.682	0.614	13.0	18.6	
Mg II λ2798	6	...	8.5	...	0.570	...	14.7	...	
Si III] λ1892 + C III] λ1909	...	9	...	15.8	...	0.437	...	24.2	$P \gtrsim 99\%$

Since the highest peaks of the cross-correlation functions are often quite asymmetric, we also give the median of the half-maximum points Δt(center) and the FWHM of the highest peak. Also shown for comparison in Figure 6 is the autocorrelation function for the 1460 Å continuum, which is virtually identical to the F_{1460}/F_{1835} cross-correlation. The fractional measurement errors for all three continuum bands are low compared to the observed fractional variability, so that the shapes of the correlations are probably not much affected by noise dilution. For both the auto- and cross-correlations, the results of the two methods are in very good agreement, especially for small lags where most of the epochs contribute to the correlation amplitudes.

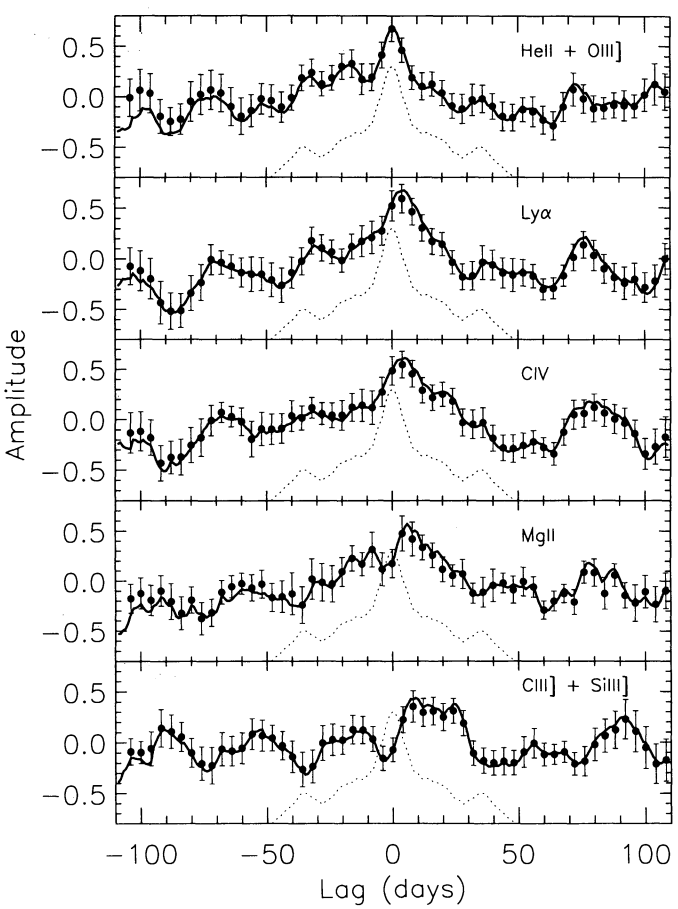

FIG. 7.—CCF and DCF correlations of various emission-line fluxes with the continuum flux at 1460 Å, based on the 4 day sampling, and calculated using the same methods as in Fig. 6. *Top to bottom:* CCFs and DCFs of the He II λ1640 + O III] λ1663, Lyα λ1216, C IV λ1549, SIPS Mg II λ2798, and Si III] λ1892 + C III] λ1909 emission features. The fluxes for all emission lines except Mg II were derived from the GEX plus spectral fitting method. Conventions are as in Fig. 6. The 1460 Å continuum ACF from Fig. 6 is also shown (*dashed line*), arbitrarily translated downward by 0.7 for clarity. Note the large values of the correlation coefficients at the peak and the very small delays of the emission lines.

The Fourier transform of the continuum ACF is the power density spectrum of the observed continuum variability. As can also be seen from the light curves, the continuum ACF shows fluctuation power on all timescales ranging from the lowest frequency to which we are sensitive, $(110 \text{ day})^{-1}$, to the highest, $(4 \text{ day})^{-1}$. Compared with NGC 5548 (Paper I), NGC 3783 appears to have relatively more high-frequency power (see § 4.2). However, as shown by the bottom panel in Figure 6, for the data set under consideration we see that even the relatively narrow core of the continuum ACF, which is due to the short-timescale flickering noted previously, is broader than the sampling window ACF. Thus, it appears that much of the variability has been resolved for this data subset.

Table 10 and Figure 6 show that the continuum bands are extremely well correlated with no detectable lag, as in the cases of NGC 5548 (Papers I and II) and NGC 4151 (Clavel et al. 1990). Correlations of the FES fluxes with the 1460 Å continuum are dominated by noise, due to the low effective S/N (ratio of standard deviation to rms uncertainty) for the FES fluxes, but are not inconsistent with zero lag. Comparison of the ultraviolet and optical continuum fluxes will be discussed elsewhere (Paper VI).

The Lyα + N V (or Lyα) and C IV cross-correlations yield the clearest results for the various emission lines. The peak amplitudes are highly significant and occur at strikingly small lags. The lag for Si IV+O IV] is similar, while the He II + O III] CCF peaks at an even shorter lag. Formally, the FWHMs for the He II + O III] and Si IV + O IV] CCFs are *less* than the FWHM for the ACF.[42] However, given the uncertainties in the correlation functions, the difference in the widths of the Si IV + O IV] and He II + O III] CCFs and the continuum ACF are probably not significant.

The value of r_{max} for the Si IV + O IV] CCF is low relative to that for the other features, but the probability that this peak is spurious is only of order 1%. Similarly, the amplitude of the

[42] The CCF is the convolution of the transfer function and the continuum ACF, so the CCF should always be broader than the ACF if the emission-line response is always positive (Sparke 1993).

Si III] + C III] CCF is rather low, but is still statistically significant at a level of confidence greater than 99%. It is worth noting that if the cross-correlation analysis is restricted to the subsets of the light curves during which the highest activity was seen (e.g., JD 2,448,660–JD 2,448,724 and JD 2,448,805–JD 2,448,833), the cross-correlation lags for Si IV + O IV], He II + O III], and Si III] + C III] are consistent with those found for the entire 7 months *and* the values of r_{max} are considerably higher on account of the higher effective "signal-to-noise ratio" of the variations relative to the random errors during the more active stages.

Both the N V and GEX-derived Mg II light curves failed to show a significant correlation with the 1460 Å continuum at any lag. However, the Mg II light curve based on the SIPS data *does* show a lag relative to the 1460 Å continuum (Table 10). On the other hand, given the differences between how the SIPS and GEX measurements were made, it is not clear whether the lag obtained for the SIPS data is due to actual variations in Mg II or to variations in the underlying ultraviolet Fe II lines. Indeed the ultraviolet Fe II lines in NGC 5548 appear to vary on about the same timescale as measured for the strong UV resonance lines (Maoz et al. 1993).

There is no widely accepted way to evaluate the uncertainties in the values of Δt(peak) and Δt(center). The analytic formula suggested by Gaskell & Peterson (1987) yields error estimates $\epsilon \lesssim 2$ days for each of the correlations summarized in Table 10, in agreement with visual inspection of the amplitude uncertainties derived by the DCF method. For well-sampled observations, Monte Carlo simulations often suggest that somewhat larger errors may be appropriate. Based on our experience with such simulations, we expect that the uncertainties in Δt(peak) are probably of order ± 2 days, while those in Δt(center) are likely to be of order 2–3 days for the stronger features (Lyα, C IV) and 3–4 days for the weaker ones (He II + O III], Mg II, Si III] + C III]).

We have repeated the above analysis for the 2 day sampling during our last 2 months of monitoring. The resulting correlations are dominated by noise and are of only marginal significance. The difference in significance is not surprising. The correlation amplitudes for the 4 day sampling are dominated by the pronounced broad "dip" at about JD 2,448,700. Inspection of Figures 6 and 7 shows that the light curves for our final 2 months of monitoring did not show similarly pronounced variations, and were more affected by relatively rapid "flickering" that we were unable to resolve even with the higher sampling rate. It is worth noting that the 1460 Å continuum ACF for the 2 day sampling is considerably narrower (FWHM $\approx$ 6–10 days) than that for the 4 day sampling (FWHM $\approx$ 14 days), in agreement with this visual impression (see Fig. 8). This indicates that the character of the continuum variability in NGC 3783 may change with time.

While most of the line-continuum cross-correlations are simply reduced in the 2 day sampling, the Si III] λ1892 + C III] λ1909 cross-correlation shows no significant correlation at all in the higher density data (Fig. 8). A plausible explanation for this is that the characteristic response timescale for Si III] + C III] (estimated at 8–30 days from the 4 day data) is too long to track the more rapid continuum variations dominating the 2 day data. If this is correct, then it would permit these data to place a lower bound on the scale of the region emitting Si III] + C III].

In summary, cross-correlation of the various continuum bands shows that over the entire observable range from 1460 to 5000 Å the continuum variations are correlated with no detectable lag (i.e., $\Delta t \lesssim 2$ days). The emission lines respond to the continuum variations with a short lag, on the order of ~0 days for He II λ1640 + O III] λ1663; ~4 days for Lyα, C IV λ1549, and Si IV + O IV] λ1402; ~9 days for Mg II λ2798; and 8–30 days for Si III] λ1892 + C III] λ1909. The results of the correlation analysis suggest that the lines characteristic of highly ionized regions (e.g., He II) respond the most rapidly. It is clear, though, that any differences in the responses of most of the emission lines are not well resolved over the mean sampling interval of the observations. What *is* clear is that the lags for NGC 3783 are considerably shorter than those derived for NGC 5548.

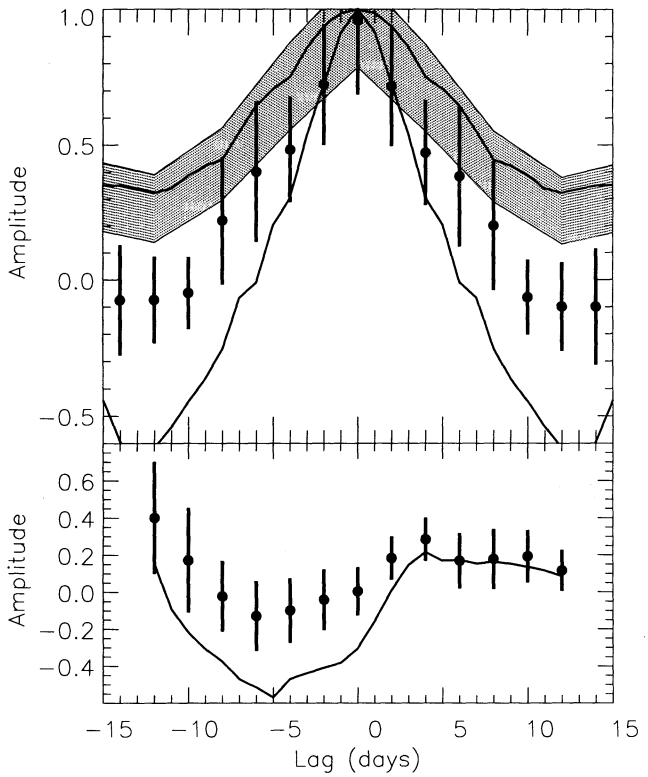

FIG. 8.—Correlations of various fluxes with the continuum flux at 1460 Å calculated for the 2 day sampling data set. All fluxes were derived from the GEX plus spectral fitting method. *Top:* Autocorrelation functions for the 1460 Å continuum fluxes. CCF amplitudes for the 2 day data are shown by the narrower, solid curve, corresponding DCF correlation amplitudes and uncertainties by the solid circles with error bars. The CCF and DCF autocorrelations for the 4 day sampling are also shown, as the enclosed solid curve and shaded area, respectively. The narrowness of the 2 day autocorrelations relative to those for the 4 day data, as well as the disagreement between the CCF and DCF amplitudes, reflect the presence of unresolved power on short timescales ($\lesssim$2 days) and indicate that the character of the continuum variability in NGC 3783 changed near the end of the monitoring campaign. *Bottom:* CCF amplitudes (*solid line*) and DCF amplitudes and uncertainties (*circles with error bars*) for the correlations of the Si III] λ1892 + C III] λ1909 fluxes with the continuum 1460 Å, for the 2 day sampling.

5. SUMMARY AND CONCLUSIONS

The nucleus of NGC 3783 has been observed intensively for 7 months using the *IUE* satellite, once every 4 days during the first 172 days and once every 2 days during the final 50 days. To date, only one other Seyfert galaxy, NGC 5548, has been as intensively studied at regular, short sampling intervals over such an extended period. As in the case of NGC 5548, signifi-

cant variations were observed in both the continuum and emission-line fluxes for NGC 3783. The character of the variability observed for NGC 3783 appears to differ in detail from that observed for NGC 5548, in that relatively rapid (i.e., faster than, or of the order of, our mean sampling intervals) fluctuations were of higher amplitude and longer-term modulations were correspondingly less well defined. However, we note the following important similarities:

1. The fractional amplitude of the continuum variations systematically decreased monotonically with increasing wavelength, from $R_{max} \approx 3.0$ at 1460 Å to $R_{max} \sim 1.5$ at ~ 5000 Å.

2. The continuum fluxes in all four ultraviolet/optical bands appear to vary simultaneously (i.e., $\Delta t < 2$ days). As a result, the continuum appears to become systematically bluer with increasing flux. As in NGC 5548, dilution by stellar light can explain at least in part why there is lower amplitude variability in the optical. Contamination by a relatively constant pseudo-continuum of blended low-contrast Fe II lines might account for $\sim 30\%$ of the observed range in ultraviolet spectral index, if NGC 3783 is similar to NGC 5548 in the properties of these contributors. We conclude that it is likely that the slope of the underlying far-UV continuum in NGC 3783 has genuinely varied.

3. The amplitude of variability of the emission lines is lower than the amplitude of the continuum, except for He II λ1640.

4. Apart from Mg II (which varied little) and N V (which is difficult to separate from Lyα), the light curves of the emission lines show marked similarities to the continuum light curves, exhibiting the initial relatively rapid fluctuations and two subsequent "dips" or local minima.

5. Cross-correlation analysis indicates strikingly short time delays for most of the strong emission lines, with the shortest delays found for the highest ionization lines. This is in agreement with the earlier results on NGC 5548. The peaks of the cross-correlation functions (relative to the 1460 Å continuum) occur at lags Δt(peak) ranging from (formally) ~ 0 days for He II λ1640 + O III] λ1663 to ~ 4 days for Lyα λ1216 and C IV λ1549. The data further suggest lags of ~ 4 days for Si IV + O IV] λ1402, and 8–30 days for Si III] λ1909. Uncertaintities in these quantities are likely to be of order 2–3 days for the stronger features (Lyα, C IV) and 3–4 days for the weaker ones (He II + O III], Si IV + O IV] λ1402, Si III] + C III]). We obtain consistent results for the lags whether we analyze the entire data set or restrict the analysis to the intervals surrounding either of the two well-defined local flux minima.

6. Both the N V and the GEX-derived Mg II light curves failed to show a significant correlation with the 1460 Å continuum at any lag. The SIPS-derived Mg II light curve *does* show a lag of ~ 9 days; it is not clear, however, whether this lag is due to actual variations in Mg II or to variations in the underlying ultraviolet Fe II lines.

7. Comparison of the autocorrelation functions for the effective 4 day sampling and 2 day sampling data sets suggests that the power density spectrum contains substantial unresolved power over timescales of $\lesssim 2$ days, and that the character of the continuum variability may change with time. The lack of correlation between Si III] + C III] and continuum fluxes in the 2 day data set may indicate that the characteristic response timescale for Si III] + C III] is too long to track the more rapid continuum variations dominating the 2-day data.

It is a pleasure to thank all of the individuals associated with the Goddard and Vilspa *IUE* observatories for their continued cooperation and support of these demanding monitoring programs. We also wish to thank our many colleagues, including the *IUE* peer review committees on both sides of the Atlantic, for their support of this effort. We especially thank the following people who supported this project in its developmental stage: B. Balick, S. Beck, J. N. Bregman, W. Brinkmann, T. J.-L. Courvoisier, D. Crampton, R. M. Cutri, M. Däther, A. Diaz, D. Dultzin-Hacyan, M. Elvis, G. J. Ferland, H. Fink, I. S. Glass, P. M. N. Hintzen, J. P. Huchra, J. B. Hutchings, A. Laor, E. Liebowitz, C. F. McKee, E. J. A. Meurs, S. Molendi, S. L. Morris, E. Rokaki, J. Roland, H. C. Thomas, Z. Tsvetanov, D. A. Turnshek, S. Veilleux, R. M. Wagner, R. J. Weymann, B. J. Wilkes, B. J. Wills, and D. Wills. We gratefully acknowledge direct financial support of this program through NASA grant NAG 5-1824 to Ohio State University and NASA contract NAS 5-32474 to Computer Sciences Corporation. Much of the data reduction was done using the Vax computer cluster at the GSFC Laboratory for Astronomy and Solar Physics. This research has made use of the NASA/IPAC Extragalactic Database (NED), which is operated by the Jet Propulsion Laboratory, California Insitute of Technology, under contract with NASA.

APPENDIX A

DERIVATION OF UNCERTAINTIES FOR FES COUNTS

The original calibration of the FES star tracker set the accuracy of measurement at about 7% (Holm & Crabb 1979; Barylak, Wasatonic, & Imhoff 1984). Since then, however, the reference point of the FES has been changed (Pérez 1991). FES counts of standard stars taken at the new reference point indicate that, for individual samples giving values of ~ 600 counts, accuracies of $\sim 10\%$ can be expected. Hence, in this range we can expect uncertainties of $\sim 0.6\%$–0.8% for averages over 300–500 samples (corresponding to half as many independent measurements; M. R. Pérez 1993, private communication). However, it is not known how the uncertainty scales with magnitude of FES counts.

We have therefore derived an empirical scaling relation for FES count uncertainty in the following way. We first assumed that the FES counts for both target and background did not vary over any 4 (or 8) hr epoch. Under this assumption, the various FES measurements during any given epoch can be taken as independent samples of two averages—the total (target plus background) and the background counts. For each epoch, we calculated the average values for the total and background counts, and the residuals of the appropriate measurements about these averages. Only those measurements made at the reference point, and averaged over many samples, were used. We then accumulated the residuals into 11 bins according to the value of the FES counts,

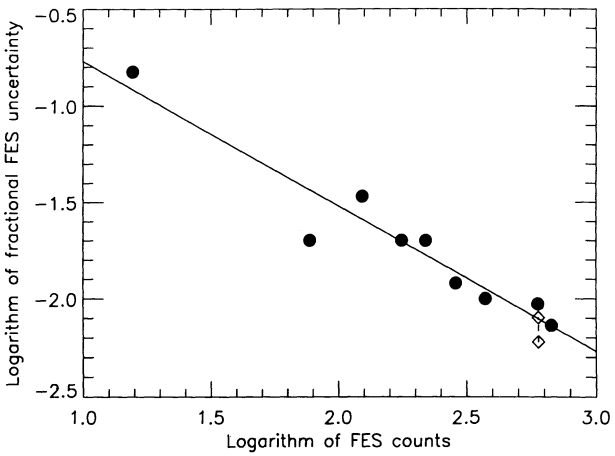

FIG. 9.—Estimated fractional uncertainty in FES counts vs. FES counts. The filled circles show the values of σ for the Gaussians that best describe the fractional residuals in FES counts, derived for several different values (see text). The open diamonds show the fractional uncertainty which we estimate should apply for a value of ~ 600 counts measured over 300 or 500 samples, scaling from single-sample measurements of standard stars and assuming that half of the samples are independent. The solid line shows the best linear fit to the logarithms and has a slope of -0.75.

and found the standard deviation σ of the Gaussian best describing the cumulative distribution of residuals for each bin. These were taken to give the total, empirical uncertainties for each range of FES counts.

Figure 9 shows these Gaussian uncertainties (σ) plotted as a function of average FES counts within each bin. The numbers of residuals within each bin are indicated. The best-fitting relation of the form

$$\sigma = A \times (\mathrm{FES})^n$$

is also plotted. The result is that σ scales as FES counts to about the $\frac{1}{4}$ power. The normalization gives an uncertainty of 0.8% at 600 counts, in good agreement with the estimate from observations of standard stars.

We have used this relation to derive uncertainties for the total and background FES counts given in Table 1 and, from these, the uncertainties in the net counts. We emphasize that the derived relation is purely empirical and may overestimate the true uncertainties if there are significant variations in either background or target count rates over timescales of hours.

APPENDIX B

FOS SPECTRAL ANALYSIS

The reduced data provided by the pipeline processing system at STScI used the most up-to-date calibration files available for the FOS, so little additional reduction was required to obtain flux-calibrated spectra. The basic pipeline reduction process first converts raw counts to count rates by correcting for the quarter-stepping, overscan, and disabled diodes. These count rates are then corrected for nonlinearities in the Digicon detectors due to paired pulses. The effects of the geomagnetically induced image motion (Junkkarinen et al. 1991) are corrected by computing the expected shift in the dispersion direction for each integration/readout period and then offsetting the spectra by integral quarter-diode steps to compensate. Background rates (predominantly induced by charged particles) were computed from a model that accounts for the dependence on geomagnetic latitude, and then subtracted. The spectra are corrected for small-scale photocathode nonuniformities using appropriate flat fields, and then converted to absolute flux by multiplying the count rates by the most recent inverse sensitivity curves. The wavelength scale is assigned based on template spectra obtained during the science verification phase of operations.

The most significant changes to this basic reduction process were to perform a more accurate background subtraction for the G130H spectra, to make a slight adjustment to the flux scale of the G190H spectrum to bring it into agreement with the G130H spectra in the region of the wavelength overlap, and to correct the assigned wavelength scale based on the positions of Galactic absorption lines. The unexposed sections of the G130H spectra below 1130 Å provide a good measure of the actual background rate. New background-subtracted spectra based on these data were produced and flux-calibrated using the CALFOS task in the FOS package of IRAF/STSDAS. The two separate G130H exposures agree to better than 0.5% in their mean flux level. A weighted average of these two spectra was taken to produce a mean G130H spectrum. The G190H spectrum was 1.0% lower in the 1578–1605 Å region of wavelength overlap, so its flux level was arbitrarily raised to bring it into agreement with the mean G130H spectrum. Numerous Galactic absorption features are visible in each spectrum. Assuming that these features are at zero average velocity, a linear shift of $+0.262$ Å was applied to each of the G130H spectra, and a shift of $+0.775$ Å was applied to the G190H spectrum.

The FOS spectrum was fitted by a model consisting of a reddened power law and emission and absorption components, as described in § 3.1. Only data in the wavelength range 1160–2150 Å were fitted; longer wavelengths were excluded to avoid the broad Fe II emission, which is difficult to model. For each emission line, the minimum number of components necessary to give an

adequate fit was used. The strongest lines with the highest S/N typically required three components (Lyα and C IV). Lines of intermediate strength could be adequately modeled with two components (Si IV, He II, and C III]), and the weakest lines all were fitted well by single Gaussians. In addition to the Galactic absorption features, Lyα and C IV absorption features intrinsic to NGC 3783 (at a small relative blueshift, $\Delta v \approx 600$ km s^{-1}) were required to obtain a good fit.

In all, 136 free parameters were determined by the 3253 data points included in the fit. The best-fit χ^2 is 3980.39. Results of the fitting procedure are summarized in Tables 2–4 and Figure 1. We note that the Galactic reddening we derive, $E_{B-V} = 0.12 \pm 0.01$ mag, is in good agreement with that inferred from the H I column (9.4×10^{20} cm^{-2}; Stark et al. 1992), i.e., $E_{B-V} = 0.13 \pm 0.04$ mag according to the prescription of Burstein & Heiles (1982).

APPENDIX C

IUESIPS AND FLUX SUMMATION METHOD

In this method we used the standard, one-dimensional spectra produced by the *IUE* Spectral Image Processing System (IUESIPS; Turnrose & Thompson 1984; Harris & Sonneborn 1987). In IUESIPS, total or "gross" (background + source) spectra are derived by summing the geometrically and photometrically corrected two-dimensional, "extended line-by-line" (ELBL; Munoz-Peiro 1985) spectral images in the cross-dispersive direction, over the 18 pixels (19".4) subtended by a point source. Data in adjacent strips are summed and smoothed to form background spectra, which are then subtracted from the total spectra to give the net source fluxes. The resulting net fluxes were calibrated using either the inverse sensitivity curves of Holm et al. (1982; SWP) or Cassatella, Lloyd, & Gonzalez-Riestra (1988; LWP), and corrected for changes in the temperature of the camera head amplifier (THDA), using the most recent correction factors (Garhart 1991). No corrections were applied to offset degradations in camera sensitivity, since these losses are negligible over the 7 months of our campaign. In contrast to the method used in Paper I, the spectra were not shifted to align strong emission lines, as the SWP and LWP spectra averaged over the entire campaign did not show broader emission-line cores than did individual spectra. No manual corrections were made to remove blemishes and cosmic-ray hits from the ELBL data.

Continuum fluxes were measured in three wavelength bands: 1445–1475 Å, 1820–1850 Å, and 2680–2720 Å (wavelengths given are as observed unless otherwise specified). These bandpasses were chosen to be as free as possible of emission-/absorption-line features, as determined by the FOS spectra. Bright spots were removed from continuum regions of the net spectra in the following way. Within each band, the median flux and a robust estimate of the standard deviation, S1, were calculated.[43] All points deviating from the median by more than 3 × S1 were then rejected, and the mean and standard deviation of the remaining fluxes computed. This has proved to be an efficient means of removing bright spots not flagged by IUESIPS.

The fluxes for the various emission lines were measured by direct integration above the continuum. No attempt was made to remove bright spots within emission-line spectral regions. The same completely impersonal and fully automated algorithm was used as in Paper I, with the difference that the continuum was (in most cases) defined as the straight line passing through two "line-free" bands adjacent to the emission line. The regions of integration were 1225–1280 Å, 1355–1460 Å, 1460–1624 Å, 1624–1710 Å, 1890–1948 Å, and 2700–2930 Å for the Lyα, Si IV + O IV], C IV, He II + O III], Si III] + C III], and Mg II lines, respectively. The Lyα λ1216 interval avoids the strong geocoronal Lyα emission line but excludes a significant fraction of flux from the blue wing of the line. Except for the Si III] + C III] feature, the underlying continuum was defined as the straight line joining the mean fluxes over the bands 1340–1370 Å and 1440–1480 Å (Lyα and Si IV + O IV]), 1440–1480 Å and 1710–1730 Å (C IV and He II + O III]), or 2680–2720 Å and 2920–2960 Å (Mg II). It was necessary to treat Si III] + C III] somewhat differently, as the IUESIPS calibration does not extend beyond 1950 Å. Hence the continuum under Si III] + C III] was assumed to be independent of wavelength, and equal to the mean flux in the range 1840–1860 Å.

Figures 10 and 11 show the regions of integration and continuum definition bands for the various emission lines, superposed on typical SWP and LWP spectra.

The resulting continuum and emission-line fluxes and their estimated uncertainties are given in Tables 5–7. Fluxes given for epochs in which more than one exposure in a camera was obtained are averages over the values from the "useful" spectra. Since Walter & Courvoiser (1991) have shown that underexposed spectra tend to be systematically low in flux as compared to adequate exposures, we have defined "useful" spectra for a given epoch to be those with integration times greater than 80% of the maximum integration time obtained in that camera during that epoch. Fluxes were only averaged over values from useful spectra. Uncertainties for the continuum and emission-line fluxes were derived by computing the standard deviations about the mean fluxes, for those epochs with more than one useful spectrum. The averages of these standard deviations were adopted as the flux uncertainties for the single-exposure epochs. Uncertainties for the multiple-exposure epochs were reduced by the square root of the number of exposures.

We caution that our continuum flux measurements will unavoidably be contaminated by some emission-line flux, due primarily to weak and blended low-contrast Fe II and Balmer continuum emission from the BLR (e.g., Wamsteker et al. 1990; Wills, Netzer, & Wills 1985). For example, Maoz et al. (1993) estimated that in NGC 5548, Fe II + Balmer continuum emission might contribute 20%–30% of the flux at 2700 Å. Hence our continuum measurements for NGC 3783 are likely to be contaminated by a similar amount.

[43] SI = $S_{\rm med}/\Phi^{-1}(0.75)$, where $\Phi^{-1}(0.75)$ is the value of the inverse standard normal function at the point 0.75, $S_{\rm med} = {\rm med}_i\,\{|x_i - x_{\rm med}|\}$, and $x_{\rm med} = {\rm med}_i\,\{x_i\}$ is the median of the data.

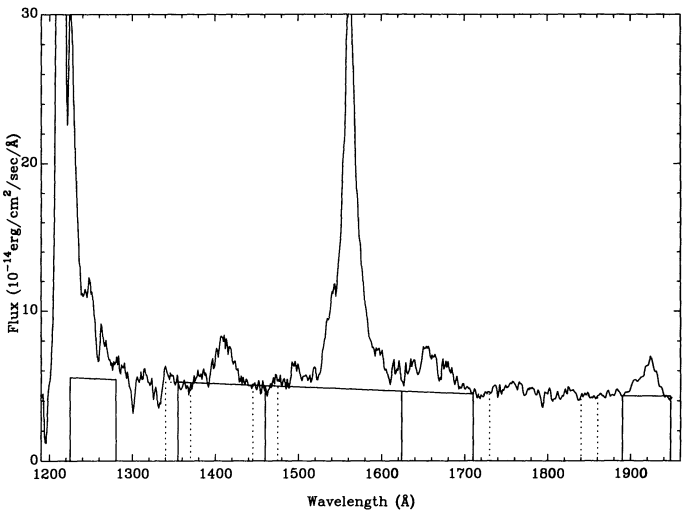

FIG. 10

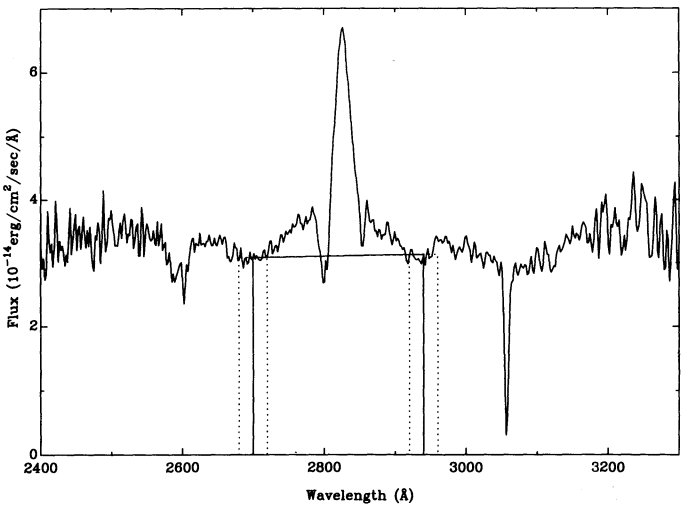

FIG. 11

FIG. 10.—Mean SIPS-extracted SWP spectrum from the *IUE* monitoring campaign. The solid vertical lines show the regions over which the emission-line fluxes were integrated. The dashed vertical lines show the regions which were used to determine the underlying continuum fluxes in the emission-line regions. The straight-line approximations to the underlying continua are also shown.

FIG. 11.—Mean SIPs-extracted LWP spectrum from the *IUE* monitoring campaign. Conventions are as in Fig. 10.

APPENDIX D

MODIFIED GAUSSIAN EXTRACTION TECHNIQUE

As in Paper I, we applied an optimizing spectral extraction method in order to improve the signal-to-noise ratio of the spectra and thus reduce the uncertainties in measurement of the weaker emission lines. The method used was the modified Gaussian extraction (GEX) technique (see discussions in Paper I and Reichert et al. 1991). Briefly, the steps taken were as follows:

1. The two-dimensional, geometrically and photometrically corrected (ELBL) files were cleaned of cosmic-ray hits and other blemishes. In the background regions, the corrections were made by calculating flux percentiles in the background regions and replacing the fluxes falling outside the upper or lower second percentiles by median values. In the source regions, the corrections were made by careful interpolations over the affected pixels.
2. The two-dimensional data were binned into large wavelength bins and fitted using Gaussian point-spread profiles plus linear background terms. Variable wavelength bins were allowed, to take advantage of regions of higher flux and/or camera sensitivity. The background and Gaussian terms were allowed to vary freely. Skewed Gaussians were fitted to the SWP data; the skewness values were fixed with wavelength according to the relation derived by Cassatella, Barbero, & Benvenuti (1985).
3. The two-dimensional data were binned into smaller wavelength bins and refitted with the Gaussian plus linear background models. In these fits, only the normalizations of the Gaussians were allowed to vary. Values of the other parameters were determined from the large-bin values according to fourth- or fifth-order polynomial fits (Gaussian widths), quadratic interpolations over wavelength (background terms), or linear interpolation (Gaussian positions).

Net spectral fluxes are given by the integrals under the Gaussian fits to the smaller bins. The resulting net fluxes were calibrated using the same sensitivity curves as for the first method, and also corrected for THDA effects using the same correction factors.

The difficulties of deriving true uncertainties for *IUE* data are well known. However, if the fitted Gaussians (or skewed Gaussians) are good representations of the cross-dispersive profiles, then, in the absence of systematic effects, it should be possible to use the deviations between the fitted models and the data as estimates of the uncertainties. As discussed in Paper I, we can check this idea by comparing these estimates with residuals about flux averages for pairs of spectra. Fortunately, for the present data set a large number of near-concurrent pairs and triples of spectra of nearly equivalent exposure quality were obtained, allowing a thorough analysis.

A total of 22 SWP and 16 LWP spectra, obtained at eight and seven epochs, respectively, which are very nearly equivalent in integration time and exposure quality were obtained during the campaign. For each epoch we have constructed average spectra and computed the residuals about these averages on a pixel-by-pixel basis. We then accumulated the residuals over six (SWP) and four (LWP) continuum wavelength ranges. In all cases, the distributions of fractional residuals (i.e., ratio of residual to average flux) are well described by Gaussians. The uncertainties of the Gaussians that best describe the observed distributions are given in Table 11; here ϵ is the derived fractional uncertainty $\langle \sigma_{\rm GEX}/F_{\rm GEX} \rangle$ and $\sigma_{\rm est}$ is the dispersion of the Gaussian that best describes the distribution of corresponding deviations about the mean. The quadrature difference between these two parameters,

$$\Delta = (\sigma_{\rm est}^2 - \epsilon^2)^{1/2} , \quad (4)$$

TABLE 11

UNCERTAINTIES IN GEX EXTRACTED FLUXES

Wavelength Range (Å)	ϵ	σ_{est}	Δ
1340–1388	0.052	0.066	0.041
1433–1483	0.062	0.070	0.032
1611–1634	0.052	0.063	0.035
1691–1783	0.038	0.052	0.036
1802–1884	0.028	0.042	0.031
1946–1975	0.029	0.043	0.032
2614–2651	0.038	0.053	0.037
2670–2724	0.036	0.050	0.034
2916–3032	0.039	0.050	0.031

shows that the distributions of residuals are somewhat broader than expected from the GEX deviations that best fit the observed distributions of residuals. Inspection shows that the observed distributions can be described by the average GEX deviations if an additional uncertainty of about 3% in the fluxes is assumed. The amount of broadening required is independent of wavelength and date of observation.

One way in which such a broadening could be introduced is through variability on short timescales (i.e., a few hours). However, multiple *IUE* exposures of white dwarf stars show similar deviations, typically of order 1%–2% when averaged over the entire spectral range, and of order 3% (or higher) when smaller wavelength bins are used (D. S. Finley 1992, private communication). Nor are spectra whose fluxes are relatively high within one wavelength bin uniformly higher over the entire spectral range. Instead, a spectrum may be relatively higher or lower from bin to bin. Similar behavior is observed when the NGC 3783 residuals are plotted against wavelength. We conclude that the additional broadening in the residuals is actually due to systematic uncertainties. Hence the GEX deviations are measures of the statistical uncertainties alone. The systematic uncertainties will need to be taken into account when deriving the uncertainties in the continuum and emission-line fluxes (see Appendix F).

Similar conclusions were reached in Paper I, based on a less detailed analysis involving fewer pairs of spectra of mostly unequal quality.

APPENDIX E

EMISSION-LINE AND CONTINUUM FITTING

E1. FITS TO THE SWP SPECTRA

Flux measurements for the emission lines and the continuum were derived from multicomponent, least-squares fits to the GEX-extracted spectra. The template for fitting the SWP spectra is based on the fit obtained for the higher resolution, higher S/N FOS spectrum (§ 3.1). We reiterate that no physical significance should be attached to any of the components listed in Tables 3 and 4. They merely serve as a convenient description of the data which fit it well and permit accurate fluxes with suitable error bars to be determined.

The relatively poorer resolution, lower S/N, and limited wavelength range of the SWP spectra led to several problems when the attempt was made to fit the FOS model to the data. Not all of the parameters in the FOS model were required by the *IUE* data. Nor could all of the parameters be adequately constrained, especially those for the weaker components, whose values proved to be interdependent. Starting values for the parameters could not be determined independently, and it was necessary to restrict the ranges of some of the parameters for the weaker lines, in order to obtain physically realistic solutions. Hence, it was necessary to modify the model and fitting procedure used for the FOS spectrum, as discussed below.

First, the model used to fit the SWP data differs somewhat from the FOS model. Over the bandpass of the fits, the SWP spectra are adequately fitted by a single power law with no extinction correction. Wavelengths redward of 1950 Å, where the SWP fluxes begin to show noticeable affects from the 2200 Å dust feature, are not included. The SWP spectral fits thus yield effective spectral indices for the reddened continuum, averaged over the bandpass of the fits. The blue wing of the Lyα line is lost in the geocoronal emission in the *IUE* data, so that the damped Lyα absorption and intrinsic Lyα absorption line are not required. No emission from C II λ1335 is required, so this component is also omitted from the *IUE* fits.

Many parameters which were permitted to vary freely in the fit to the FOS spectrum were fixed at constant values, or explicitly linked to other parameters in the fit. The wavelengths of the Galactic absorption features were linked to the peak of the C IV emission line, and their full widths at half-maximum were fixed at the resolution of *IUE* (Cassatella et al. 1985). Galactic absorption lines with equivalent widths less than 1 Å (as measured from the FOS spectrum) were also fixed in equivalent width. The relative widths of the medium and broad components of Lyα were fixed at the ratio derived from the FOS spectrum, and the N V width was linked to these. The wavelengths of each of these features were also linked to the wavelength of C IV, although their fluxes were permitted to vary freely. Within the Si IV + O IV] blend, the C IV, He II, and O III] blend, and the Si III] + C III] blend, the relative wavelengths and widths of individual components were also linked, but the overall width and wavelength of each blend were free to vary. For the weakest lines, O I λ1302, N IV] λ1486, and N III] λ1750, the full widths at half-maximum were fixed at the values obtained in the fit to the FOS spectrum.

To derive initial parameter guesses for each individual spectrum, we first fitted the *IUE* model to the mean spectrum for the whole campaign. For each individual spectrum, the initial continuum flux was then scaled to match that measured in the 1445–1470 Å window. An estimate of the C IV line flux was obtained by subtracting this continuum from a direct integration over the 1500–1600 Å window. All initial guesses for emission-line fluxes were then scaled by the ratio of this C IV flux estimate to the C IV flux in the mean spectrum. Corrections to the wavelength scale were determined by measuring the peak of the C IV emission line. We assume that this wavelength did not vary throughout the campaign, and that any deviations are due to centering of the active nucleus in the *IUE* aperture. This approach is justified since (*a*) the Lyα peak moves in the same manner as the C IV peak throughout the campaign, and (*b*), for the strongest Galactic absorption features (S II + Si II at 1260 Å and C II λ1335) in the highest S/N spectra, these lines also shift in wavelength in concert with the C IV emission-line peak.

The fitted parameters were constrained to lie within a pre-selected range. In practice, the only significant boundary imposed on any parameter was the restriction that emission-line fluxes and absorption-line equivalent widths be greater than or equal to zero. The χ^2 for each fit was minimized in several stages that alternated between a Simplex algorithm and a Levenberg-Marquardt algorithm. Within a given stage the boundary conditions imposed on the parameter are soft, i.e., excursions beyond the boundary are permitted, but the parameter is set back to the boundary value at the beginning of each new iteration and permitted to vary freely again. At the start of subsequent stages, however, hard limits are imposed on any parameter which is outside the selected boundary. The parameter is then set to the boundary value and fixed at that limit. This results in slightly different numbers of freely varying parameters for each fit, depending on how many parameters were fixed at a boundary. Examples of such occurrences are fits in which the flux of a weak emission line such as O I λ1302 or N IV] λ1486 are set equal to zero.

Fits were done in a stepwise fashion which decoupled parameters that were not closely linked. We first fitted the continuum alone in the windows 1340–1380 Å plus 1750–1890 Å. With the continuum fixed, we fitted the Si IV + O IV] blend, then the Si III] + C III] blend, and then the C IV and He II + O III] spectral region. Once nearly final values had been determined for each of the parameters

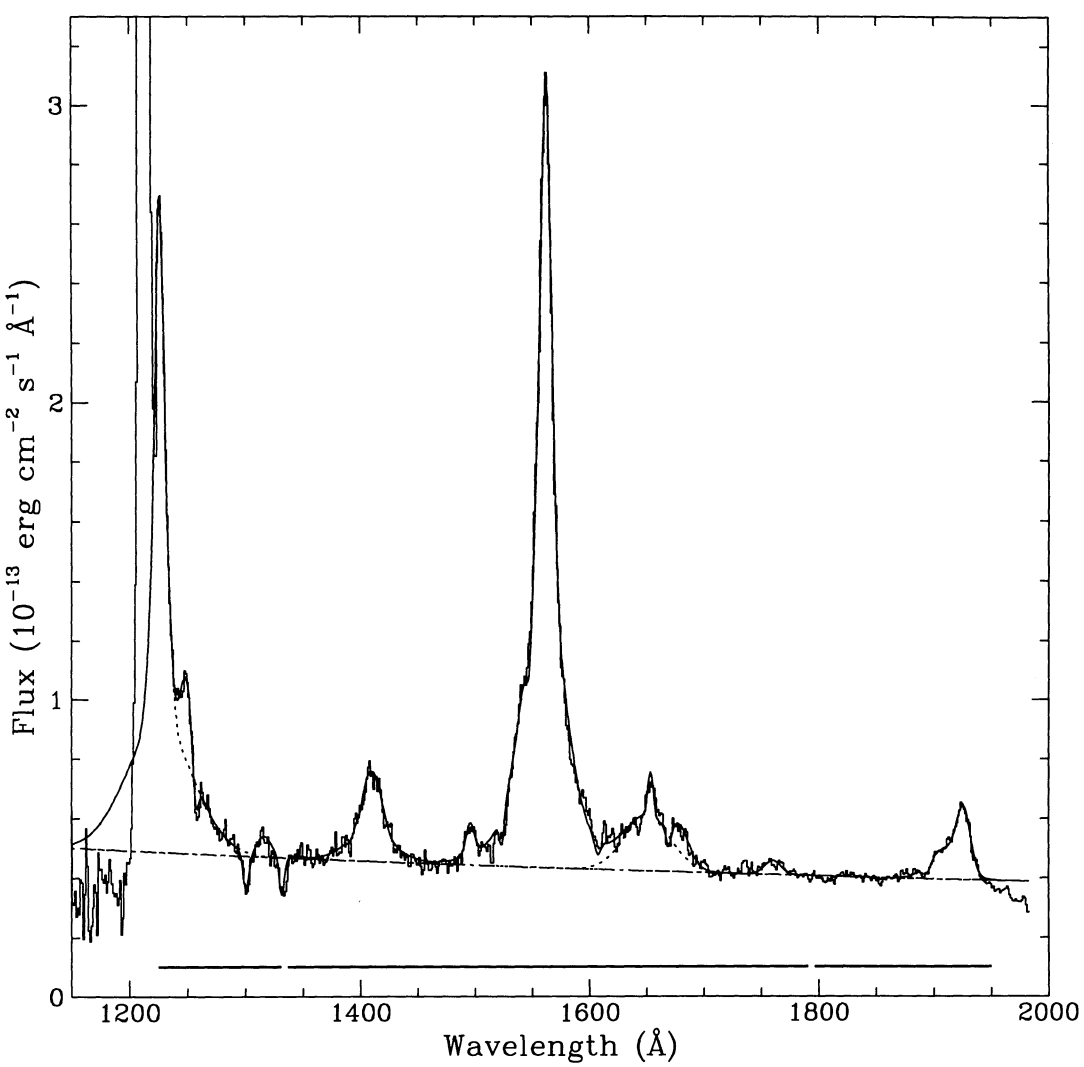

FIG. 12.—Mean SWP spectrum, averaged over the entire monitoring campaign. The heavy horizontal solid-lines show the wavelengths which were included in the fits. The smooth solid curve shows the best model fit; the short-dashed lines show the sums of the components for Lyα and He II + O III]. The underlying power-law fit to the continuum is also shown.

in the independent line complexes, we fitted the spectral range from 1327 to 1950 Å with all line and continuum parameters free to vary. Small regions from 1792 to 1796 Å and from 1896 to 1911 Å were excluded from the fit to avoid reseaux.

The Lyα region is difficult to measure accurately, since there is no good continuum shortward of Lyα and since the blue wing of Lyα is contaminated by geocoronal emission. We fixed the continuum parameters at the values determind by fits over the wavelength range 1327–1950 Å. Fits to the Lyα region spanned the wavelength range 1225–1370 Å, excluding a reseaux at 1322–1326 Å.

Figure 12 shows a plot of the mean SWP spectrum, averaged over all of the observations. The best-fit model is also shown.

E2. FITS TO THE LWP SPECTRA

Fits to the LWP spectra are complicated by the pseudocontinuum of Fe II emission, which is present throughout the LWP spectral range. The strongest groups of multiplets are easily seen in most of the LWP spectra. Comparing these with a model of Fe II emission (Netzer & Wills 1983) shows that the 2680–2720 Å wavelength interval is at a minimum in the Fe II emission. There is a strong "bump" just to the blue of Mg II λ2798, and the brightest feature in the models of Netzer & Wills (1983) lies directly under the Mg II emission line.

Unfortunately, we were unable to obtain FOS spectra covering the LWP wavelength range. It was therefore necessary to resort to theoretical calculations when building our fitting models. To avoid the complications of modeling the entire Fe II spectrum, only the region from 2400 to 3030 Å was fitted. Strong Galactic absorption lines due to Fe and Mn in the windows 2551–2624 Å and 2901–2959 Å proved difficult to model consistently, so these regions were also excluded. A power law was fitted to the underlying pseudocontinuum. The Fe II emission was modeled using a synthetic spectrum from Netzer & Wills (1983) convolved with a profile matching the C IV emission line. Strong blends of Fe II emission centered at observed wavelengths 2541, 2815, and 2994 Å were not well matched by the Netzer & Wills (1983) model, and additional broad Gaussians were added at these wavelengths to give a good fit. The amplitudes of these Gaussians were determined by scaling the Gaussian component at 2994 Å to match the data; the 2541 and 2815 Å Gaussian components were then scaled so that the three relative heights matched those in the Netzer & Wills (1983) model. The Mg II λ2798 emission line was modeled with with three Gaussian components. The width of the narrowest was fixed at the *IUE* resolution of 900 km s^{-1}. Two Gaussian absorption lines for the strong Galactic Mg II λλ2796, 2803 doublet were also included. The full widths at half-maximum of the two absorption lines were fixed at the *IUE* resolution, their equivalent widths at the values derived from the fit to the mean LWP spectrum (2.07 and 2.42 Å, respectively), and their relative wavelengths according to their laboratory values. For the limited wavelength range used in the LWP fits, it proved difficult to obtain consistent fits in which the power-law index was allowed to vary freely. We also expect the LWP slopes to differ from those for the SWP, owing to the strengths of the Fe II and Balmer continuum emission. We therefore fixed the LWP index at the value obtained for the fit to the

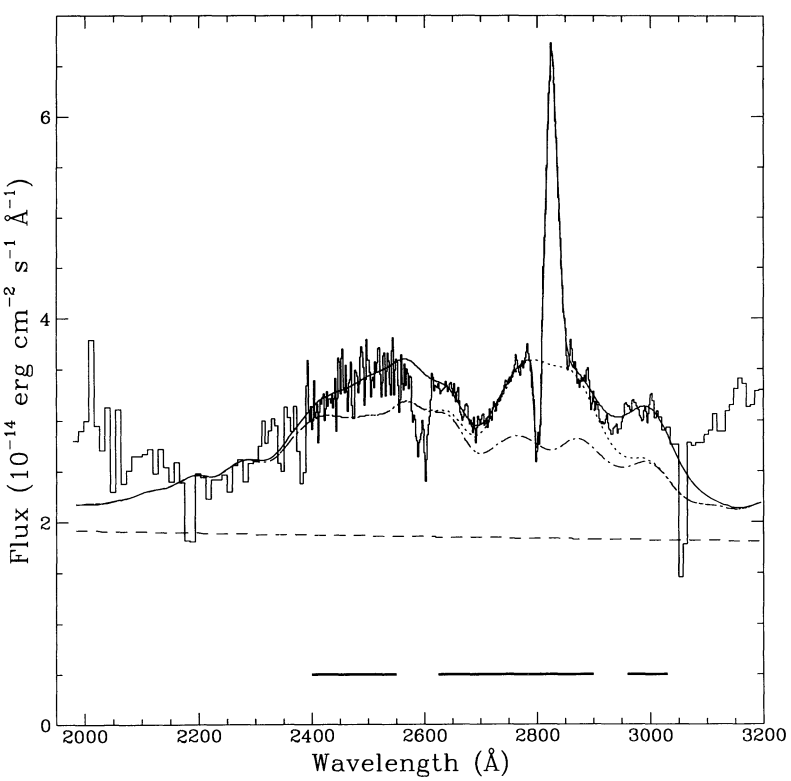

FIG. 13.—Mean LWP spectrum, averaged over the entire monitoring campaign. The heavy horizontal solid lines show the wavelengths which were included in the fits. The smooth solid curve shows the best model fit. The dot-dash curve shows the best-fitting Fe II model, based on the model of Netzer & Wills (1983), while the dotted curve shows the extra three components of Fe II which were needed to achieve a good fit to the data. Note that the sum of these three components can make up much of the broad base underlying Mg II. The underlying power-law fit to the continuum is shown by the long-dashed line.

mean LWP spectrum and used $F_\lambda \propto \lambda^{-0.123}$. In fitting an individual LWP spectrum, the line fluxes were fixed and the continuum flux normalized using the wavelength ranges 2400–2450 Å, 2695–2725 Å, and 3000–3030 Å, to avoid the Mg II line and the strongest Fe II blends. Next, the continuum was fixed and only the line fluxes permitted to vary. Finally, all line and continuum parameters were permitted to vary freely in the final fit.

Figure 13 shows a plot of the mean LWP spectrum, averaged over all of the observations. The best-fit model is also shown. The contribution from the three Fe II blends at 2541, 2815, and 2994 Å is also shown. Note that in this characterization of the data, the broad "bump" which underlies the three Mg II Gaussians is attributed almost entirely to Fe II. Although this is a highly model-dependent separation, it is not physically unreasonable. If the broad bump were due entirely to Mg II, it would have a velocity width of 30,000 km s^{-1}, far broader than any of the other broad-line components and in particular broader than the broadest C IV λ1549 component. The widths of the broad Mg II components in our model, on the other hand, are in good agreement with the widths of the broad components for the other lines.

APPENDIX F

UNCERTAINTIES FROM EMISSION-LINE AND CONTINUUM FITTING

Uncertainties in the values of the fitted parameters in both the SWP and LWP spectra were calculated in a semiempirical way. Under the assumption that each parameter is a single "interesting" parameter (Avni 1976), the 1 σ error σ_i on a parameter a_i is obtained from the error matrix of the fit ϵ_{ij}:

$$\sigma_i^2 = \epsilon_{ii} .$$

For observed quantities of interest which are functions of more than one parameter, e.g., the total flux of C IV, the uncertainty is calculated using

$$\sigma^2 = \sum_i \sigma_i^2 + \sum_{i \neq j} \sigma_{ij}^2 ,$$

where the cross variance σ_{ij}^2 is the error matrix element ϵ_{ij}.

Typically the reduced χ^2 for the fits, χ_ν^2, ranged from 3 to 6, indicating that the statistical uncertainties for the individual fluxes (derived from the deviations about the cross-dispersive profiles in the Gaussian extractions) probably underestimate the true uncertainties by a factor of $\sim$2. As discussed by Reichert et al. (1992), this is likely due to correlations between adjacent points in the spectra, so that the effective number of degrees of freedom in the fits are a factor of $\sim$3 less than the actual number. We determined the appropriate scaling factor for each set of fits independently by fitting a theoretical χ^2 distribution with a reduced number of degrees of freedom to the observed χ^2 distributions from the LWP fits, the SWP fits in the 1327–1950 Å range, and the SWP fits in the 1225–1350 Å range. The derived scale factors are 3.55, 5.05, and 3.52, respectively. The error bars for each flux were then scaled by the square root of the appropriate scale factor.

The error bars at this point represent internal statistical errors. We next make some estimate of external and systematic errors, which will include variations due to placement of the object in the aperture, the history of the exposure of each camera, and the inherent repeatability of *IUE* flux measurements. As noted in Appendix D, multiple exposures of calibration standards with *IUE* show systematic uncertainties of order 1%–2%, and this is corroborated by the GEX-extracted fluxes. Hence we assign an intrinsic repeatability error of 2% to each individual spectrum, and add this linearly as a systematic error to each of our flux measurements. The only exceptions to this are the uncertainties in spectral index. Since these are primarily based on flux ratios internal to a single spectrum, the apparently random repeatability errors should cancel to first order.

We tested the appropriateness of the errors in the line and continuum fluxes in two ways: (1) by examining the scatter in the results for multiple observations that were obtained during the same *IUE* shift, and (2) by looking at the power spectra of each measured quantity for the whole campaign. Under the assumption that there is no variability on timescales as short as a single *IUE* shift, the differences in line or continuum flux for the spectral pairs should have a Gaussian distribution with zero mean and dispersion comparable to the root mean square of the sums in quadrature of the error bars for each pair of measurements. The results of the comparison are given in Table 12, which lists the weighted mean flux and weighted dispersion about the mean for each feature. The values of σ for the Gaussians which best describe the distributions of the flux differences from the spectral pairs are also given. It is encouraging that the observed distributions have dispersions that are of the same order as the predicted dispersions.

The power spectra for each measured quantity were computed from a linear interpolation of the measured quantities at 1 day intervals. The power spectra are generally steep, and the signal merges into the noise at frequencies of $\sim$0.25 day^{-1}, as expected since our sampling interval was generally every 4 days. The mean value of the power spectrum from 0.25 day^{-1} to the Nyquist frequency indicates the mean square of the noise level. These estimates of the noise levels for the various quantities are also given in Table 12. Inspection of Table 12 shows that, while the dispersions from the spectral pairs tend to be higher than our derived uncertainties, the estimated noise levels from the power spectrum analysis tend to be lower. The agreement between the various uncertainty estimates is very good for the continuum fluxes, and still within a factor of 2 or so for the emission-line fluxes and spectral indices. We conclude that the uncertainties derived from our fits are of the right order of magnitude and represent a reasonable compromise between those estimated by the other methods. We caution, however, that we have not proved that the errors follow Gaussian distributions in detail; care should be exercised if one is using them in statistical tests which assume normal distributions.

TABLE 12

UNCERTAINTIES IN GEX-DERIVED QUANTITIES

FEATURE	QUANTITY				POWER SPECTRUM NOISE
	⟨Flux⟩	σ(flux)	$\langle\sigma_{GEX}\rangle$	$\sigma(\Delta Flux_{ij})$	
F_{1460}	4.66	0.87	0.12	0.24	0.12
F_{1835}	3.06	0.63	0.10	0.20	0.07
F_{2700}	1.85	0.47	0.25	0.10	0.08
C IV λ1549	706	55	41	55	16
Si III] λ1892 + C III] λ1909	62.1	11.2	5.1	20.2	4.1
Lyα λ1216	520	67	44	65	18
N V λ1240	40.1	16.5	7.5	23.3	69
Si IV λ1400 + O IV] λ1402	80.5	15.9	9.4	19.4	4.7
He II λ1640 + O III] λ1663	114	32	11.7	32.6	7.7
O I λ1302	9.6	5.0	7.0	10	2.7
N IV] λ1486	9.6	4.2	4.1	6.3	1.5
N III] λ1750	9.7	3.8	3.5	5.2	1.5
Mg II λ2798	8.1	7.0	6.2	5.2	1.0
F_0	4.86	1.65	0.33	0.80	0.26
α_ν	1.40	0.30	0.072	0.23	0.063

[a] Values for continuum fluxes are given in units of 10^{-14} ergs cm^{-2} s^{-1} Å^{-1}; for emission lines, in units of 10^{-14} ergs cm^{-2} s^{-1}.

REFERENCES

Alloin, D., et al. 1994, in preparation
Avni, Y. 1976, ApJ, 210, 642
Barr, P., Willis, A. J., & Wilson, R. 1983, MNRAS, 202, 453
Barylak, M., Wasatonic, R., & Imhoff, C. 1984, ESA *IUE* Newsletter, 20, 201
Blandford, R. D., & McKee, C. F. 1982, ApJ, 255, 419
Boggess, A., et al. 1978a, Nature, 275, 2
———. 1978b, Nature, 275, 7
Burstein, D., & Heiles, C. 1982, AJ, 87, 1165
Carini, M. T. 1991, NASA *IUE* Newsletter, 46, 23
Cassatella, A., Barbero, J., & Benvenuti, P. 1985, A&A, 144, 335
Cassatella, A., Lloyd, C., & Gonzalez-Riestra, R. 1988, NASA *IUE* Newsletter, 35, 225
Chapman, G. N. F., Geller, M. J., & Huchra, J. P. 1985, ApJ, 297, 151
Clavel, J. 1991, in Variability of Active Galactic Nuclei, ed. H. R. Miller & P. J. Wiita (Cambridge: Cambridge Univ. Press), 301
Clavel, J., et al. 1990, MNRAS, 246, 668
Clavel, J., et al. 1991, ApJ, 366, 64 (Paper I)
Collin-Souffrin, S. 1991, A&A, 249, 344
Courvoisier, T. J.-L., & Clavel, J. 1991, A&A, 248, 389
Crenshaw, D. M., & Blackwell, J. H., Jr. 1990, ApJ, 358, L37
de Ruiter, H. R., & Lub, J. 1986, A&AS, 63, 59
de Vaucouleurs, G., de Vaucouleurs, A., & Corwin, H. G. 1976, Second Reference Catalogue of Bright Galaxies (Austin: Univ. Texas Press)
Dietrich, M., et al. 1993, ApJ, 408, 416 (Paper IV)
Edelson, R. A., & Krolik, J. H. 1988, ApJ, 333, 646
Evans, I. N. 1989, ApJ, 338, 128
Faelker, J., Gordon, F., & Sandford, M. C. W. 1987, in Exploring the Universe with the *IUE* Satellite, ed. Y. Kondo, W. Wamsteker, A. Boggess, M. Grewing, C. de Jager, A. L. Lane, J. L. Linsky, & R. Wilson (Dordrecht: Reidel), 21
Ferland, G. J., Peterson, B. M., Horne, K., Welsh, W. F., & Nahar, S. N. 1992, ApJ, 387, 95
Garhart, M. P. 1991, NASA, *IUE* Newsletter, 46, 65
Gaskell, C. M., & Peterson, B. M. 1987, ApJS, 65, 1
Gaskell, C. M., & Sparke, L. S. 1986, ApJ, 305, 175
Glass, I. S. 1992, MNRAS, 256, 23P
Harris, A. W., & Sonneborn, G. 1987, in Exploring the Universe with the *IUE* Satellite, ed. Y. Kondo, W. Wamsteker, A. Boggess, M. Grewing, C. de Jager, A. L. Lane, J. L. Linsky, & R. Wilson (Dordrecht: Reidel), 729
Holm, A. V., Bohlin, R. C., Cassatella, A., Ponz, D. P., & Schiffer, F. H. 1982, A&A, 112, 341
Holm, A. V., & Crabb, W. G. 1979, NASA *IUE* Newsletter, 7, 40
Horne, K., Welsh, W. F., & Peterson, B. M. 1991, ApJ, 367, L5
Junkkarinen, V., Beaver, E., Cohen, R., & Lyons, R. 1991, Instr. Sci. Rep. CAL/FOS-066
Koratkar, A. P., & Gaskell, C. M. 1991, ApJS, 75, 719
Krolik, J. H., Horne, K., Kallman, T. R., Malkan, M. A., Edelson, R. A., & Kriss, G. A. 1991, ApJ, 371, 541
Maoz, D., et al. 1993, ApJ, 404, 576
Marshall, N., Warwick, R. S., & Pounds, K. A. 1981, MNRAS, 194, 987
McHardy, I. 1988, Mem. Soc. Astron. Ital., 59, 239
Menzies, J. W., & Feast, M. W. 1983, MNRAS, 203, 1
Munoz-Peiro, J. R. 1985, NASA *IUE* Newsletter, 27, 27
Netzer, H., & Maoz, D. 1990, ApJ, 365, L5
Netzer, H., & Wills, B. J. 1983, ApJ, 275, 445
Pérez, M. R. 1991, NASA *IUE* Newsletter, 45, 19
Peterson, B. M. 1991, in Variability of Active Galaxies, ed. W. J. Duschl, S. J. Wagner, & M. Camenzind (Berlin: Springer-Verlag), 47
———. 1993, PASP, 105, 247
Peterson, B. M., et al. 1991, ApJ, 368, 119 (Paper II)
Peterson, B. M., et al. 1992, ApJ, 392, 470 (Paper III)
Pogge, R. W., & Peterson, B. M. 1992, AJ, 103, 1084
Press, W. H., & Teukolsky, S. A. 1992, Computers in Physics, Vol. 6, No. 3 ("Numerical Recipes" column)
Reichert, G. A., Branduardi-Raymont, G., Filippenko, A. V., Mason, K. O., Puchnarewicz, E. M., & Wu, C.-C. 1992, ApJ, 387, 536
Reichert, G. A., et al. 1991, in Variability of Active Galactic Nuclei, ed. H. R. Miller & P. J. Wiita (Cambridge: Cambridge Univ. Press), 335
Seaton, M. J. 1979, MNRAS, 187, 73P
Sparke, L. S. 1993, ApJ, 404, 570
Stark, A. A., Gammie, C. F., Wilson, R. W., Bally, J., Linke, R. A., Heiles, C., & Hurwitz, M. 1992, ApJS, 79, 77
Stirpe, G. M., de Bruyn, A. G., & van Groningen, E. 1988, A&A, 200, 9
Stirpe, G. M., et al. 1994, ApJ, 425, 609 (Paper VI)
Teays, T. 1991, NASA *IUE* Newsletter, 45, 1
Turner, T. J., Nandra, K., George, I. M., Fabian, A. C., & Pounds, K. A. 1993, ApJ, 419, 127
Turnrose, B. E., & Thompson, R. W. 1984, *International Ultraviolet Explorer* Image Processing Information Manual, Version 2.0 (New Software) (CSC/TM-84/6058; Silver Spring: Computer Sciences Corporation)
Ulvestad, J. S., & Wilson, A. S. 1984, ApJ, 285, 439
Unger, S. W., Lawrence, A., Wilson, A. S., Elvis, M., & Wright, A. E. 1987, MNRAS, 228, 521
Walter, R., & Courvoisier, T. J.-L. 1991, A&A, 250, 312
Wamsteker, W., et al. 1990, ApJ, 354, 446
Weinstein, D., & Carini, M. 1992a, NASA *IUE* Newsletter, 48, 143
———. 1992b, NASA *IUE* Newsletter, 49, 5
Wills, B. J., Netzer, H., & Wills, D. 1985, ApJ, 248, 472
Winge, C., Pastoriza, M. G., Storchi-Bergmann, T., & Lipari, S. 1992, ApJ, 393, 98